DENSE MOLECULAR GAS AND DUSTY TORUS IN NGC 4303

Ángel A. Soní[1], Irene Cruz-González[1], Martín Herrera-Endoqui[1,2], Erika Benítez[1], Yair Krongold[1], and Arturo I. Gómez-Ruiz[3]

ABSTRACT

Spectrum analysis at 3 mm of the central region ($r \approx 800$ pc) of NGC 4303 showed molecular gas lines of both dense gas tracers (HCN, HNC, HCO$^+$, and C$_2$H) and diffuse gases (^{13}CO and C^{18}O). Molecular gas parameters: H_2 mass M_{H_2}=(1.75±0.32)×10^8 M$_\odot$; radial velocity V$_{dense}$ =178±60 km s^{-1}, and V$_{CO}$=151±29 km s^{-1}; HCN luminosity L_{HCN}=(7.38±1.40)×10^6 K km s^{-1} pc^2; dense gas mass M_{dense}=(4.7±0.3)×10^7 M$_\odot$, indicating a significant contribution of dense to total molecular gas mass. To explore the AGN nature and central dusty torus of the galaxy, CIGALE was used to fit the integrated spectral energy distribution. Large torus properties are estimated: luminosity L_{TORUS} = (7.1±2.8)×10^{43} erg s^{-1} and line of sight inclination of 67±16°, which is consistent with a Type 2 AGN; total infrared luminosity L_{IR}=(3.51 ± 0.30)×10^{44} erg s^{-1}; star formation rate SFR=6.0±0.3 M$_\odot$ yr^{-1}. A marginal AGN contribution of ≈20% was found.

RESUMEN

El análisis del espectro a 3 mm de la región central ($r \approx 800$ pc) de NGC 4303, mostró líneas de trazadores de gas molecular denso HCN, HNC, HCO$^+$ y C$_2$H, y difuso ^{13}CO y C^{18}O. Se obtuvo: masa del H_2 M_{H_2}=(1.75 ± 0.32)×10^8 M$_\odot$; velocidad radial de gas denso V_{dense} =178 ± 60 km s^{-1}, y gas difuso V_{CO} =151 ± 29 km s^{-1} luminosidad de HCN L_{HCN}=(7.38 ± 1.40)×10^6 K km s^{-1} pc^2, masa de gas denso M_{dense}=(4.7 ± 0.3)× 10^7 M$_\odot$, i. e., contribuye significativamente a la masa total del gas molecular; y abundancias de trazadores de gas denso. Se utilizó CIGALE para ajustar la distribución espectral de energía integrada y explorar la actividad y el toro de polvo central. Para el toro se obtuvo: luminosidad L_{TORUS} = (7.1±2.8)×10^{43} erg s^{-1} y ángulo de visión 67±16°, i. e., AGN tipo 2; luminosidad total infrarroja L_{IR}=(3.5±0.3)×10^{44} erg s^{-1}; tasa de formación estelar SFR=6.0 ± 0.3 M$_\odot$ yr^{-1}. Se halló que la contribución del AGN es marginal, ≈20%.

Key Words: galaxies: active — galaxies: individual: NGC 4303 — galaxies: ISM

1. INTRODUCTION

Molecular gas characterization of the few central kiloparsecs region of galaxies is important to understand how the gas is accreted into the supermassive black hole (SMBH), and the role of it in the host galaxy evolution (e.g. Costagliola et al. 2011; Jiménez-Donaire et al. 2019). The activity in the nuclei of galaxies (AGN) can be dominated by SMBH accretion or starburst (SB) processes, which have different physical and chemical properties that affect their interstellar medium (ISM).

In some AGN the obscuration of the nuclear region by dust and gas is parametrized by the neutral hydrogen column density N_H. Infrared and submillimeter observations are less susceptible to dust, especially in the 3 mm window, where the brightest emission lines such as HCN or HCO$^+$ trace dense molecular gas, whereas the ^{12}CO line traces diffuse gas. These lines have proven useful to understand the central ISM in nearby galaxies (for example,

[1]Instituto de Astronomía, Circuito Exterior, C. U., Universidad Nacional Autónoma de México, 04510 CdMx, México.

[2]Estancia Posdoctoral por México, CONAHCYT, Coordinación de Apoyos a Becarios e Investigadores.

[3]CONAHCYT-Instituto Nacional de Astrofísica Óptica y Electrónica, Luis E. Erro 1, 72840 Tonantzintla, Puebla, México.

Costagliola et al. 2011; Aladro et al. 2015). On the other hand, in the infrared the dust emission can be observed and studied using broad-band photometry.

Simultaneous observations of ^{12}CO isotopic varieties ^{13}CO and C^{18}O in galaxies are valuable for understanding the relationship between the bulk of molecular gas and its environment influenced by the SMBH accretion (e.g., García-Burillo 2016). In addition, these lines are crucial for deriving the gas mass that will be converted into stars.

Furthermore, observations of molecular dense gas tracers such as HCN, HNC, HCO$^+$, CS, and N$_2$H are valuable because their critical densities are of the same order as the molecular cloud cores, which are the star formation sites. Such studies base their analysis on the emission line ratios; for example, HCN/HCO$^+$ has been used as a discriminator between AGNs, segregating them into non-Seyfert galaxies (nuclear SB) or pure Seyfert (Sy) galaxies (Kohno 2003). Additionally, HCN/HCO$^+$ has been used as an indicator of the presence of AGNs, although this has been challenged several times without conclusive evidence (e.g., Costagliola et al. 2011; Privon et al. 2020). HCN/HNC has been used to characterize photon-dominated regions (PDRs) and X-ray dominated regions (XDRs) (e.g., Meijerink et al. 2007). In addition, both ratios show variations between different galaxy locations such as the center, disk, spiral arms and interarm regions in different studies (e.g., Bigiel et al. 2016; Jiménez-Donaire et al. 2019; Sorai et al. 2019; Morokuma-Matsui et al. 2020). Finally, the dense to diffuse gas ratio HCN/^{12}CO associated to star-forming regions is used as a proxy for the dense gas fraction, f_{dense}, as in Neumann et al. (2023).

In the study of dense gas tracers the HCN luminosity (L_{HCN}) can be converted to dense gas mass (M_{dense}), which has been linked by a tight correlation with the far-infrared luminosity, which is closely correlated to the star formation rate (SFR): $L_{HCN} \propto M_{dense} \propto L_{FIR} \propto SFR$ (see for example, Gao & Solomon 2004a; Jiménez-Donaire et al. 2019; Neumann et al. 2023). This relationship has been observed in individual molecular clouds in the Milky Way and in nearby galaxies (Wu et al. 2005; Graciá-Carpio et al. 2006; Bigiel et al. 2008; Wu et al. 2010; Usero et al. 2015; Bigiel et al. 2016; Jiménez-Donaire et al. 2019), and also in a few distant galaxies ($z \geq 1$). Before the work of Rybak et al. (2022) only two SF galaxies and three quasar hosts exhibited HCN emissions. These authors showed the difficulties of detecting HCN at z=2.5-3.3, but concluded that the HCN/FIR ratios found were consistent with normal starburst galaxies, but not with ultraluminous ones (c.f., their Figure 5).

Additional information about the properties of the gas in the central kiloparsecs of galaxies can be obtained studying other emission mechanisms that occur inside those spatial scales, such as AGNs. According to the Unified AGN model (see Antonucci 1993; Urry & Padovani 1995), the key to distinguish between Seyfert 1 and 2 galaxies is the existence of a dust structure surrounding the central engine that obscures the inner parts of the AGN on the line of sight (LOS). Based on its geometric shape this structure is called a dusty torus; however, different distributions have been proposed for dust, such as those in Fritz et al. (e.g., 2006); Nenkova et al. (e.g., 2008); Hönig & Kishimoto (e.g., 2017). The contribution of the dusty torus luminosity to the integrated spectral energy distribution (SED) could be estimated by an SED fitting analysis (e.g., Ciesla et al. 2015; Miyaji et al. 2019) which yields the dusty torus properties together with the galaxy continuum and line-emitting components, as well as the contribution of the AGN. As part of a study of nearby galaxies with obscured AGN, we analyzed the molecular gas spectra in the 3 mm band of the central region (1.6 kpc in diameter), of the galaxy NGC 4303 (M 61). NGC 4303 is a barred spiral in the Virgo supercluster at z =0.00522 ($D_L = 16.99$ Mpc; $1'' = 81$ pc (Wright 2006)), with an inclination of $25°$ (Frei et al. 1996), classified as SAB(rs)bc (de Vaucouleurs et al. 1991). Its nuclear activity has been debated, as Huchra et al. (1982) classified it as a LINER, whereas Filippenko & Sargent (1985) as a Seyfert 2, which was confirmed by Veron-Cetty & Veron (1986) based on an equivalent width (EW) of [NII] of 400 km s^{-1}. Jiménez-Bailón et al. (2003) used Chandra images with a central radius of 3 pc and showed that in this X-ray region, both a core source (either an AGN or ultraluminous x-ray source) with a hydrogen column density $N_H \approx 1 \times 10^{20}$ cm^{-2}, and an annular starburst region of radius $3''$, which is more obscured with $N_H \approx 5 \times 10^{21}$ cm^{-2}, coexist. The AGN characterization of NGC 4303 was confirmed using an infrared color-color diagram (Colina et al. 2015) and BPT diagrams (Malkan et al. 2017). Furthermore, Esparza-Arredondo et al. (2020) suggested that the nucleus is a candidate for the AGN fading phase.

The AGN contribution in NGC 4303 will be studied by analyzing the continuum emission from UV to far-infrared wavelengths. The dusty torus properties provide important parameters that complement the molecular gas characterization of the central 1.6 kpc region studied in this paper. Our aim is to obtain

parameters of the interstellar medium in NGC 4303, such as the molecular gas mass, HCN gas luminosity, far-infrared luminosity and star formation rate.

The remainder of this paper is organized as follows: § 2 describes the observational details of the 3 mm band spectroscopy. § 3 presents the data reduction. An analysis of the molecular line emission spectra of NGC 4303 is described in § 4. The spectral energy distribution (SED) characterization to study the dusty torus and AGN contribution is presented in § 5. The discussion of results is given in § 6. A summary of the main conclusions and final remarks is presented in § 7. Throughout our work we adopt a cosmology where H_0=69.6 km s^{-1} Mpc^{-1}, Ω_m=0.286 and Ω_λ=0.714 (Bennett et al. 2014).

2. OBSERVATIONS

Observations of NGC 4303 were obtained on June 28 and December 22, 2015, with the Redshift Search Receiver (RSR) on the Large Millimeter Telescope Alfonso Serrano (LMT), henceforth RSR/LMT, in its early science phase, which operated with a 32-m active surface. Observing conditions at the Volcán Sierra Negra site were good most of the time. During the observations the opacity at the Volcán Sierra Negra site at a frequency of 225 GHz was in the range of $\tau = 0.18$ - 0.19. The system temperature, T_{sys}, was between 85 and 110 K. Observations were centered on the coordinates of the galaxy nucleus (α_{2000}: 12^h:21^m:54^s.9, δ_{2000}: +04°:28$'$:25$''$), with the OFF beam 39 arcsec apart. The pointing accuracy was better than 2$''$. The total ON source integration time for NGC 4303 was 1 hr.

The RSR is an autocorrelator spectrometer with a monolithic microwave integrated circuit system that receives signals over four pixels, simultaneously covering the frequency range 73 to 111 GHz at $\Delta\nu = 31$ MHz spectral resolution, which corresponds to ≈ 100 km s^{-1} at 90 GHz (see Erickson et al. 2007). Hence, across the whole 3 mm band, the velocity resolution changes from 125 km s^{-1} to 85 km s^{-1}. The RSR/LMT-32m has an angular resolution or beam full width at half-maximum (FWHM) that is also frequency dependent, ranging from 28 to 19 arc seconds, between the frequencies 73 and 111 GHz.

3. REDUCED SPECTRA

Autocorrelations, spectral co-adding, calibration, and baseline removal were performed using the *Data REduction and Analysis Methods in Python* (DREAMPY) software developed by Gopal Narayanan for the RSR. After removing integrations with unstable bandpass, the remaining spectra were averaged, weighted by the RMS noise in each individual spectrum. A simple linear baseline was removed in each spectral chassis, which covered a section of 6.5 GHz of the total RSR bandwidth after masking strong emission lines. To convert the antenna temperature (T_A) units to flux units (Jy), we used a conversion factor G, the gain of the LMT-32m, given by

$$G(\nu) = 7 \left(\frac{\nu \, [GHz]}{100 \, [GHz]} \right) [Jy \, K^{-1}]. \qquad (1)$$

The spectral reduction last step was to obtain the main beam temperature (T_{mb}). To convert antenna temperature to T_{mb}, we divided the spectrum by the main beam efficiency (η_{mb})

$$\eta_{mb} = \left(1.2 \, \exp(\nu/170)^2 \right)^{-1}, \qquad (2)$$

where ν denotes the sky frequency of the observed line. Equation (2), was obtained from calibration observations performed in June and December 2015. Details of the RSR/LMT data reduction can be found in several studies, for example Snell et al. (2011); Lee et al. (2014); Yun et al. (2015); Cybulski et al. (2016).

The RSR covers a frequency range of 84 - 111 GHz in the rest frame of NGC 4303. The entire RSR spectrum is shown in Figure 1, together with the identified lines. The RMS of the spectrum varies slightly across the frequency band from 0.618 mK at the low-frequency end ($\nu > 92$ GHz) to 0.854 mK at the high-frequency end. Several molecular spectral lines are clearly detected in this spectrum. Using a 3σ detection threshold on the line integrated intensity and rest frequencies from the *Splatalogue*[4], we detected seven spectral lines: C_2H at 87.31 GHz N=1–0, which is a blend of 6 lines: J=3/2-1/2 (F=1-1, 2-1, 1-0) and J=1/2-1/2 (F=1-1, 0-1, 1-0); HCN(1-0), HCO$^+$(1-0), HNC(1-0), CS(2-1), C^{18}O(1-0), and ^{13}CO(1-0) at 88.63, 89.18, 90.66, 109.78 and 110.20GHz, respectively, and the possible detection of three additional lines: N_2H^+ at 93.17 GHz, NH$_2$CN at 99.75 GHz and ^{13}CN at 108.65 GHz.

We note that the OFF beam position of the RSR/LMT observations falls within the main body of the galaxy; however, after careful inspection of the reduced data, we found that the ^{13}CO(1-0) spectra do not exhibit an absorption feature, which would appear if the 39 arcsec OFF beam were affected by the OFF galaxy emission. Contamination from the galaxy in the OFF position would be produced
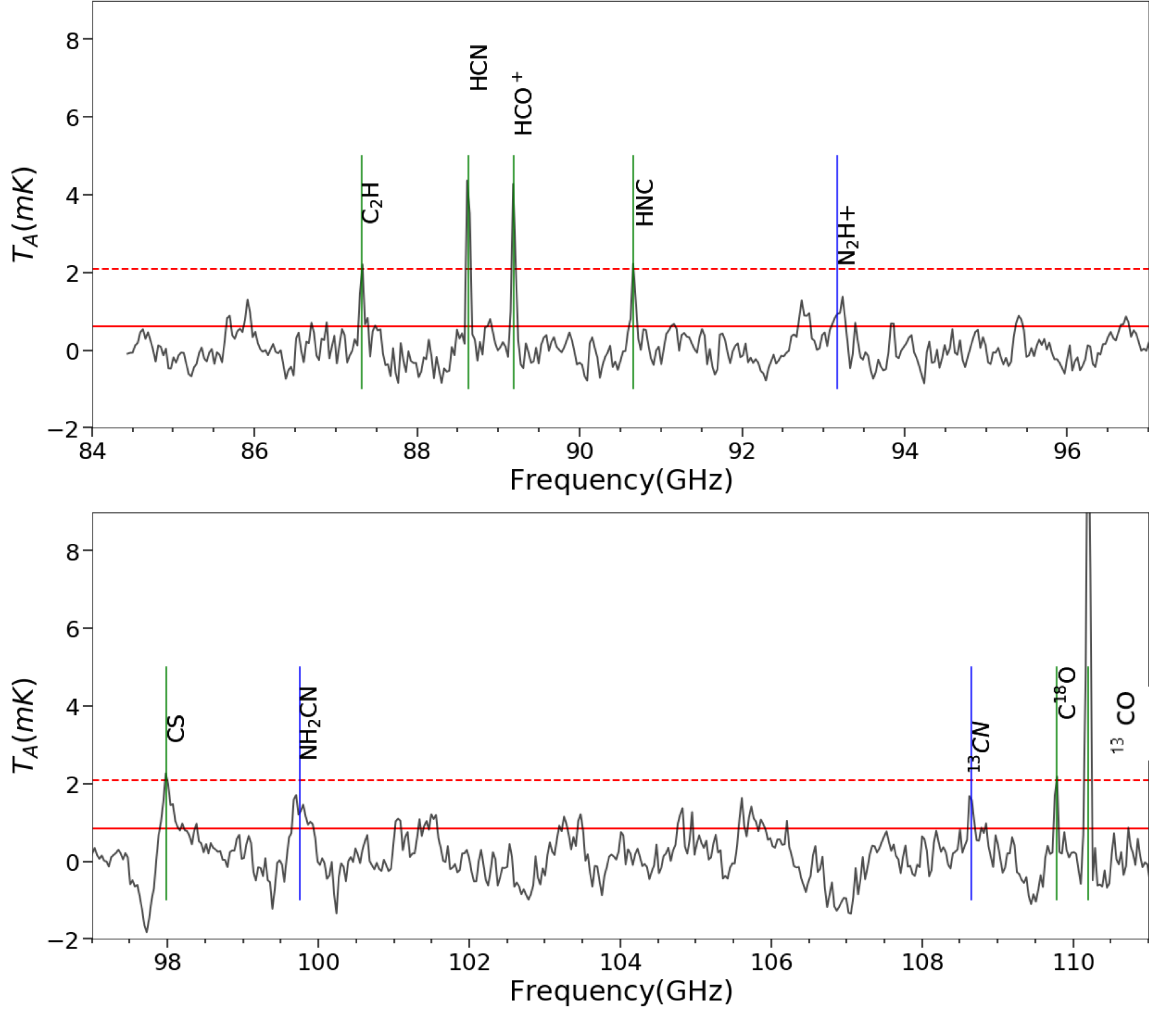
---

[4]https://splatalogue.online/#/home.

Fig. 1. NGC 4303 rest-frame spectra from 84 to 111 GHz obtained with the Redshift Search Receiver (RSR/LMT). The vertical color lines indicate the likely frequencies of some molecular transitions. The red solid line indicates the root mean square (RMS) value in each panel. The red dashed line represents the value of 3σ. Note that the detected transitions, vertical green lines, are detections of C_2H, HCN, HCO^+, HNC, CS(2-1), $C^{18}O$, and ^{13}CO, whereas the possible detections, vertical blue lines, are N_2H^+, NH_2CN and ^{13}CN (see Table 1). The color figure can be viewed online.

by faint CO emission in the spiral arms or inter-arm regions, c.f., PHANGS-ALMA CO(2-1) image of NGC 4303 in Leroy et al. (2021) and would affect all lines, dense and diffuse. This is not found in any of the lines detected, so contamination, if present, is small.

4. ANALYSIS

4.1. Molecular Gas

Seven molecular lines were measured to have integrated line intensity with $S/N > 3$, but CS(2-1) which shows a drop at the low-frequency end, was considered a marginal detection, and so is not in-

cluded in the line analysis. For each line, a single Gaussian fit was performed to obtain the integrated intensity, calculated in a range of -250 to $+250\,\mathrm{km\,s^{-1}}$, centered on their rest frequencies. The error was computed using the covariance matrix of the fit. The FWHM and peak intensities were obtained using fitting parameters. Individual plots of the detected lines are shown in Figure 2 and the derived parameters are listed in Table 1.

The most intense line is $^{13}CO(1-0)$ followed by HCN, HCO^+ and HNC. In a previous study on molecular gas in NGC 4303, Yajima et al. (2019) detected integrated intensities similar to those re-

TABLE 1

MOLECULAR LINE TRANSITIONS DETECTED IN NGC 4303

Molecule	Frequency[b]	Integrated Flux	Δv^{c}	Peak Intensity[d]
	(GHz)	(K km s^{-1})	(km s^{-1})	(mK)
(1)	(2)	(3)	(4)	(5)
C$_2$H(1-0)	87.31	0.77±0.03	192±38	3.47±0.96
HCN(1-0)	88.63	1.55±0.11	138±59	9.28±0.97
HCO^{+}(1-0)	89.18	1.41±0.09	171±73	6.98±0.97
HNC(1-0)	90.66	0.90±0.04	225±48	3.47±0.98
CS(2-1)[a]	97.98	<2.03±0.68^{e}	–	–
C^{18}O(1-0)	109.78	0.77±0.04	146±28	4.37±1.54
^{13}CO(1-0)	110.20	4.53±0.26	155±29	24.45±1.55

Notes:

[a]Possible detection.

[b]Rest frequencies, obtained from the Splatalogue database at https://splatalogue.online/#/home.

[c]FWHM in velocity units.

[d]Peak intensity of main beam temperature (T$_{MB}$).

[e]Upper limit; because line has a blue absorption feature the integrated flux and error are large (see Figure 1).
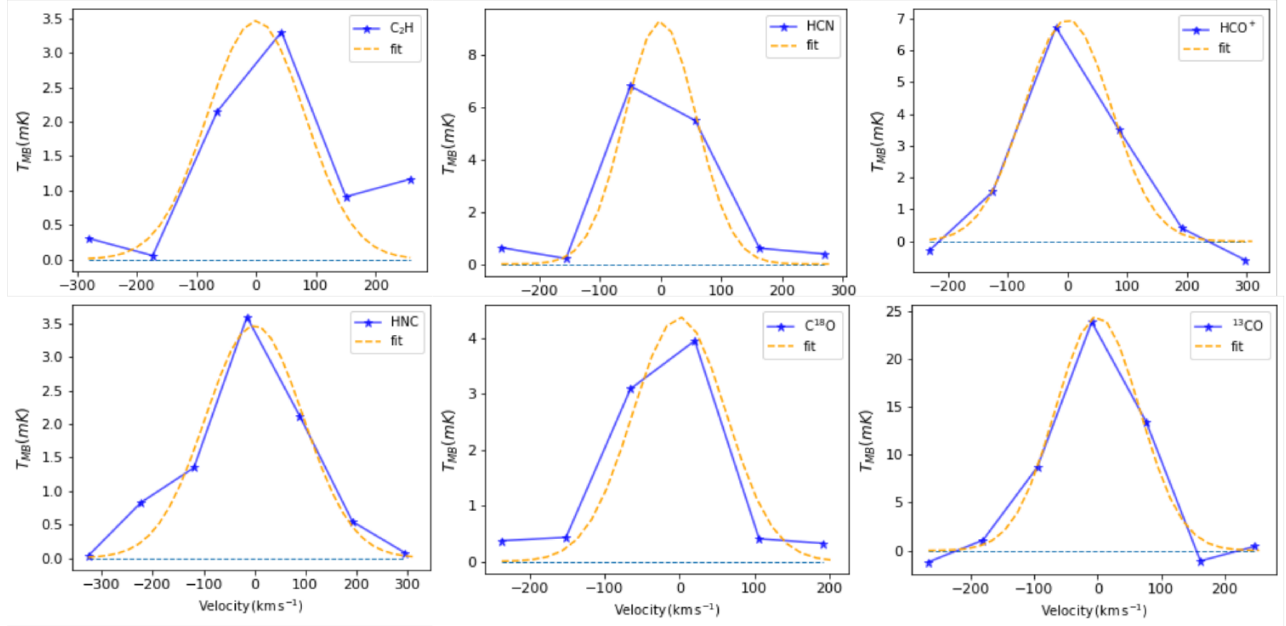

Fig. 2. Observed (blue) molecular lines with $S/N > 3$ of NGC 4303 and their Gaussian fits (orange dashed lines). We detected dense gas tracers as well as ^{12}CO isotopic varieties. From left to right the molecular lines are as follows: (top row) C^{2}H, HCN, HCO^{+}; (bottom row) HNC, C^{18}O and ^{13}CO. The color figure can be viewed online.

ported here for ^{12}CO(1-0) and ^{13}CO(1-0) using the Nobeyama 45 m radio telescope, but they were not able to detect C^{18}O(1-0). Also, Li et al. (2021) detected the same dense gas tracer lines (HCN, HCO^{+}, HNC) with the IRAM 30 m and reported integrated measurements similar to those of this work.

In the following steps, we calculate the mass of the dense molecular gas in the central 1.6 kpc. First, with a combination of optically thin and thick lines, optical depth can be derived. Then, we calculate the column density to finally use it in the calculation of the molecular gas mass. Following Jiménez-

Donaire et al. (2017), and assuming local thermodynamic equilibrium (LTE), solar abundances and a given excitation temperature in a cloud, the optical depth (τ_{13}) for ^{13}CO can be calculated from the integrated intensities of ^{12}CO and ^{13}CO, I_{12} and I_{13}, respectively. Assuming the beam-filling factor of each line to be the same in the equation of radiative transfer, the optical depth is:

$$\tau_{13} = -\ln\left[1 - \frac{I_{13}}{I_{12}}\right]. \qquad (3)$$

Because ^{12}CO in NGC 4303 cannot be detected in the frequency range of our observations, we used the value $I_{12} = 55.2 \pm 5.5$ K km s^{-1} obtained with the EMIR spectrograph at the IRAM 30m telescope (FWHM beam size 22″) reported by Israel (2020) and I_{13} derived from our spectra[5]. Using the values in equation (3) yields $\tau_{13} = 0.09 \pm 0.01$, that is, an optically thin line. For ^{12}CO, the optical depth is calculated by multiplying τ_{13} by the relative solar abundance[6] [^{12}CO/^{13}CO] = 89 (Wilson & Rood 1994), which yields $\tau_{12} = 7.12 \pm 0.89$; that is, the ^{12}CO line is optically thick.

Now, we used the integrated intensity I_{13} and τ_{13} to obtain the column density N_{13}. Equation (4) is the result of using the radiative transfer equation to calculate the number of molecules of ^{13}CO over a path length (see equation 1.7 in Jiménez-Donaire 2017):

$$\left[\frac{N_{13}}{cm^{-2}}\right] = 3 \times 10^{14} \left[\frac{I_{13}}{K\,km\,s^{-1}}\right]\left[\frac{1}{1-e^{-\tau_{13}}}\right] \frac{\tau_{13}}{1-e^{-5.29/T_{ex}}}. \qquad (4)$$

Three excitation temperature (T_{ex}) values commonly found in dense molecular clouds, 10, 20 and 30 K, are assumed in equation (4) for the subsequent calculations.

To obtain the mass of H_2, it was necessary to convert N_{13} to $N(H_2)$ using the following equation:

$$\left[\frac{N(H_2)}{cm^{-2}}\right] = \left[\frac{H_2}{^{13}CO}\right]\left[\frac{N_{13}}{cm^{-2}}\right], \qquad (5)$$

where the relative abundance was [H_2/^{13}CO] = 588,235 (Dickman 1978). Finally, the H_2 mass was obtained from equation (6) assuming a spherical cloud with a diameter calculated for

_____

[5] The difference in beam size of 3″ between the two telescopes is small, and might not strongly affect the LMT value of I_{13} used, also it is unlikely that $\tau_{13} > 1$.

[6] This is the value that most studies assume, but it can vary by a factor of 4.5 between galaxy centers, the local ISM or the solar system.

TABLE 2

COLUMN DENSITIES OF ^{13}CO AND H$_2$ AND $M(H_2)$

T_{ex} [K]	N_{13} [$\times 10^{15}$cm^{-2}]	$N(H_2)$ [$\times 10^{21}$cm^{-2}]	$M(H_2)^*$ [$\times 10^7 M_\odot$]
10	3.44 ± 0.63	2.02 ± 0.37	6.88 ± 1.26
20	6.08 ± 1.11	3.58 ± 0.65	12.17 ± 2.23
30	8.74 ± 1.60	5.14 ± 0.94	17.50 ± 3.20

Note: $^*M(H_2)$ was calculated from equation (6).

the telescope main beam, which for the ^{13}CO line is 20″, which at the distance of NGC 4303 corresponds to a diameter $d = 1.647$ kpc; m_{H_2} is the molecular mass of H_2,

$$M(H_2) = \frac{\pi d^2}{4} N(H_2)\,m_{H_2}. \qquad (6)$$

The derived parameters for NGC 4303 are presented in Table 2, which includes the column densities N_{13}, $N(H_2)$ and mass $M(H_2)$ for the three values of T_{ex}.

To obtain the total molecular gas mass (M_{mol}), the contribution of molecular helium to molecular hydrogen must be included in the relationship $M_{mol} \approx 1.36\,M(H_2)$ from Teng et al. (2022). Therefore, for $T_{ex} = 30$ K we obtain $M_{mol} = (2.38 \pm 0.43) \times 10^8$ M$_\odot$. To derive the amount of gas in the observed region, we calculated the surface density of the molecular gas (Σ_{mol}), which is the mass of H_2 per square parsecs area. Taking M_{mol} and the equivalent area of a circle of 1647 pc in diameter, the total surface density of molecular gas is $\Sigma_{mol} = 112 \pm 20$ M$_\odot$ pc^{-2}.

Using the same procedure as described above, we obtained the total molecular gas mass and surface density of the molecular gas for $T_{ex} = 10$ K, that is, $M_{mol} = (9.35 \pm 1.71) \times 10^7$ M$_\odot$ and $\Sigma_{mol} = 46.5 \pm 8.5$ M$_\odot$ pc^{-2}. Within this range of possible values of T_{ex}, Σ_{mol} varies by a factor of 2.

Usero et al. (2015) calculated the surface density of molecular gas from the intensity of ^{12}CO using the following equation:

$$\Sigma_{mol}[M_\odot\,pc^{-2}] = \alpha_{CO}\,I_{12}\cos(i), \qquad (7)$$

where i is the inclination of the galaxy, and α_{CO} is the conversion factor of ^{12}CO to molecular gas mass with an adopted value of 4.4 M$_\odot$pc^{-2}(K km s^{-1})$^{-1}$ (including the 1.36 factor for helium), with a ±30% uncertainty given by Bolatto et al. (2013). Using I_{12} from literature, we obtain $\Sigma_{mol} = 220 \pm 79$ M$_\odot$ pc^{-2}.

Analogously, we calculated the surface density of the dense molecular gas traced by the HCN line using the equation:

$$\Sigma_{dense}[M_{\odot}\,pc^{-2}] = \alpha_{HCN}\,I_{HCN}\cos(i), \quad (8)$$

where $\alpha_{HCN} = 10$ M$_{\odot}$ pc^{-2} (K km s^{-1})$^{-1}$, proposed by Gao & Solomon (2004b) is a typical upper limit for spiral galaxies[7]. The result is Σ_{dense}=14±1 M$_{\odot}$ pc^{-2}.

We calculate the dense gas mass as traced by HCN, M_{dense}, by multiplying Σ_{dense} by the area of the telescope's main beam, with a diameter of 25″ for the HCN line. The result is: $M_{dense} = (4.7 \pm 0.3) \times 10^7$ M$_{\odot}$.

Finally, with Σ_{dense} and Σ_{mol} for $T_{ex} = 30$ K, we can calculate the dense molecular fraction (f_{dense}) in the observed region as:

$$f_{dense} = \frac{\Sigma_{dense}}{\Sigma_{mol}} = 0.13 \pm 0.06. \quad (9)$$

4.2. Luminosities

Gao & Solomon (2004b) calculated the luminosity of an extended source with a size larger than the main beam of the telescope. Because the galaxy is not mapped along the major axis, it is considered a source with a size equal to or smaller than the telescope's main beam. The calculation is given by:

$$L'_{HCN}\,[K\,km\,s^{-1}\,pc^2] \approx \Omega_{mb}\,I_{HCN}\,D_L^2\,(1+z)^{-3}, \quad (10)$$

where Ω_{mb} is the solid angle of the main beam, D_L(pc) is the luminosity distance, I_{HCN} is the integrated HCN line intensity and z is the redshift. We can rewrite Ω_{mb} in terms of the antenna parameters, that is, the FWHM of the main beam $\theta_{\rm FHWM}$ (in radians) and obtain the HCN luminosity as

$$L'_{HCN}\,[K\,km\,s^{-1}\,pc^2] \approx \frac{\pi}{4\,ln(2)}\theta_{\rm FHWM}^2\,I_{HCN} \\ D_L^2\,(1+z)^{-3}. \quad (11)$$

We then calculate the luminosity of the dense gas tracers substituting the integrated intensities of this work, e.g., HCN by HCO$^+$ and the corresponding values of $\theta_{\rm FHWM}$ at the observing frequency, $\approx$25″ for the dense gas tracers and 20″ for ^{13}CO (see Table 3).

---

[7]Leroy et al. (2017) reported an extensive analysis of the use of millimeter-wave emission line ratios to trace molecular gas density. In the dense gas conversion factors, they considered a range of densities for the models as well as the distribution of widths and temperatures.

TABLE 3

LUMINOSITIES FOR DIFFUSE AND DENSE GAS EMISSION LINES IN NGC 4303

Line	L_{gas} $\times 10^6$ [K km s^{-1} pc^2]	$\log(L_{gas})$ [K km s^{-1} pc^2]
^{13}CO	9.60 ± 3.90	6.98 ± 0.09
C$_2$H	3.78 ± 0.68	6.58 ± 0.07
HCN	7.38 ± 1.40	6.87 ± 0.08
HCO$^+$	6.63 ± 1.24	6.82 ± 0.08
HNC	4.09 ± 0.75	6.61 ± 0.08
Total dense	21.88 ± 4.07	7.34 ± 0.08

If we use the mass-luminosity conversion factor defined as $\alpha_{^{13}CO}$ with units M$_{\odot}$ pc^{-2} (K km s^{-1})$^{-1}$, we can rewrite the Solomon relation (Solomon et al. 1997) as $M(H_2) = \alpha_{^{13}CO}\,L'_{13}$ or

$$\alpha_{^{13}CO} = \frac{\Sigma_{H_2}}{I_{13}}. \quad (12)$$

Using the previously calculated data for $M(H_2)$, Σ_{H_2} =82±15 M$_{\odot}$ pc^{-2} and equation (12), we calculated both the factor $\alpha_{^{13}CO}$ and the ^{13}CO luminosity, obtaining $\alpha_{^{13}CO}$ = (18.2 ± 4.4) M$_{\odot}$ pc^{-2} (K km s^{-1})$^{-1}$ and L'_{13} = (9.6 ± 3.9) × 10^6 K km s^{-1} pc^2. The ^{12}CO luminosity was calculated with equation (7) and the FWHM of 22″ of the observed line, which results in L'_{12} = 1.29 × 10^8 K km s^{-1} pc^2.

To estimate the abundance of molecular gas in the nuclear obscured region, we used the integrated intensity of the different emission lines of dense gas tracers (C$_2$H, HCN, HNC and HCO$^+$), diffuse gas tracers (^{13}CO, C^{18}O) and ^{12}CO integrated intensity $I_{12} = 55.2 \pm 5.5$ K km s^{-1} (Israel 2020) to calculate their line ratios (Table 4).

4.3. Dusty Torus, SFR and AGN Contribution to the SED

As mentioned in § 1, previous multiwavelength studies confirmed that the nuclear activity of NGC 4303 is influenced by an accreting SMBH (Filippenko & Sargent 1985; Veron-Cetty & Veron 1986; Malkan et al. 2017; Colina et al. 2015), classifying it as Sy 2 (Véron-Cetty & Véron 2006). In this work we are also interested in the physical properties of NGC 4303, mainly the star formation rate (SFR), in order to compare the values derived here with those from the literature. A good tool to achieve this task is integrated spectral energy distribution (SED) fitting analysis, which includes an AGN component. Interestingly, this complementary analysis allows us

TABLE 4

ABUNDANCES OF DENSE GAS RELATIVE TO
DIFFUSE AND DENSE GAS TRACERS

Ratio[*]	Value
C_2H / $C^{18}O$	1.01 ± 0.07
HCN/ $C^{18}O$	2.01 ± 0.18
HCO^+/ $C^{18}O$	1.83 ± 0.15
HNC / $C^{18}O$	1.17 ± 0.08
CS / $C^{18}O$	2.67 ± 0.19
^{13}CO/ $C^{18}O$	5.88 ± 0.46
HCN / ^{12}CO	0.028 ± 0.002
HCO^+ / ^{12}CO	0.025 ± 0.003
HNC / ^{12}CO	0.016 ± 0.003
^{13}CO / ^{12}CO	0.082 ± 0.010
$C^{18}O$ / ^{12}CO	0.013 ± 0.002
HNC/ HCN	0.58 ± 0.04
HCO^+ / HCN	0.91 ± 0.08
C_2H / HCN	0.38 ± 0.04

Note: [*] For ^{12}CO we used $I_{12} = 55.2 \pm 5.5$ K km s^{-1} (Israel 2020).

to obtain not only the galactic properties but also the AGN properties, including dusty torus characteristics. All these properties are useful for follow-up studies.

For this purpose, we used the Code Investigating GALaxy Evolution , called CIGALE, developed by Boquien et al. (2019), which allows fitting the SED of galaxies using different models for the relevant physical components. For instance, it is possible to select from different star-forming history models, stellar populations, initial mass functions, attenuation laws, dust emissions and AGN models. The different components are fitted to preserve the energy balance principle, which means that the energy absorbed at UV and optical wavelengths is re-emitted at infrared wavelengths. To select the best fit, CIGALE performs a minimization of the χ^2 statistics and a Bayesian analysis to determine the probability distribution of the physical parameters obtained from the fits.

We searched for photometric data of NGC 4303 in the literature, using the VizieR photometry tool[8], which allows visualization of photometric points extracted from catalogues in ViZieR around a sky position. We used a default search radius of 5″ centered on NGC 4303, which is small enough to consider data truly corresponding to the emission of the

galaxy; we found multi-wavelength observations at UV, optical, infrared and sub-millimeter wavelengths (see Table 5). According to de Vaucouleurs et al. (1991), the isophotal dimensions (R_{25}) of NGC 4303 are $6.'46 \pm 0.'15$ and $5.'75 \pm 0.'27$, for the major and minor axes, respectively. This means that all the observations retrieved form the literature include the total emission of the galaxy.

The UV data consist of Galaxy Evolution Explorer (GALEX; Martin et al. 2005) observations in the far-ultraviolet (FUV; $\lambda_{eff} = 0.153$ μm) and near-ultraviolet (NUV; $\lambda_{eff} = 0.231$ μm) bands with an angular resolution of $5.''3$ and a $1°2$ field of view (FOV), taken from Cortese et al. (2012). The optical data consist of observations from the Sloan Digital Sky Survey Data Release 7 (SDSS-DR7; Abazajian et al. 2009) in the five bands u, g, r, i and z, taken from Kim et al. (2014). These data have an angular resolution of $\leq 1.''5$, and a 3° FOV. In the IR regime we compiled data from different sources: the Two Micron All Sky Survey (2MASS; Skrutskie et al. 2006), the Spitzer Space Telescope (Werner et al. 2004), the Infrared Astronomical Satellite (IRAS; Neugebauer et al. 1984), the Wide-field Infrared Survey Explorer (WISE; Wright et al. 2010), and the Herschel Space Telescope (Pilbratt et al. 2010). In the case of 2MASS data, we used photometry in the J (1.2 μm), H (1.6 μm) and K (2.2 μm) bands from Bai et al. (2015), Dalya et al. (2016) and Stassun (2019), respectively, all of them with an angular resolution of 2″ and a 8°5 FOV. In the case of Spitzer data, we considered observations obtained with the InfraRed Array Camera (IRAC; Fazio et al. 2004) in the IRAC1 (3.6 μm), and IRAC2 (4.5 μm) bands from Sheth et al. (2010), and IRAC4 (8 μm) band from Ciesla et al. (2014). These data have resolutions of $1.''7$, $1.''6$, $1.''9$, respectively, with a 5′ FOV for IRAC1 and IRAC2 bands, and $5.'2 \times 5.'2$ for IRAC4. In the case of IRAS data, we used the photometry in the 12 μm band from Moustakas & Kennicutt (2006), in the 25 and 60 μm bands from Rahman et al. (2006), and in the 100 μm band from Yun et al. (2001), with a resolution of $0.'5$, $0.'5$, $1.'0$ and $2.'0$, respectively, and a common $63.'6$ FOV. We also considered data in the MIPS 24 and 160 μm bands from Bendo et al. (2012), whose angular resolution is 6″ with a $5.'4 \times 5.'4$ FOV. From WISE, we used observations in the W1 (3.4 μm) and W2 (4.6 μm) bands from Stassun (2019), the W3 (12 μm) band from Ciesla et al. (2014), and the W4 (22 μm) band from Boselli et al. (2014). These data have angular resolution of $6.''1$, $6.''4$, $6.''5$, $12.''0$, respectively,
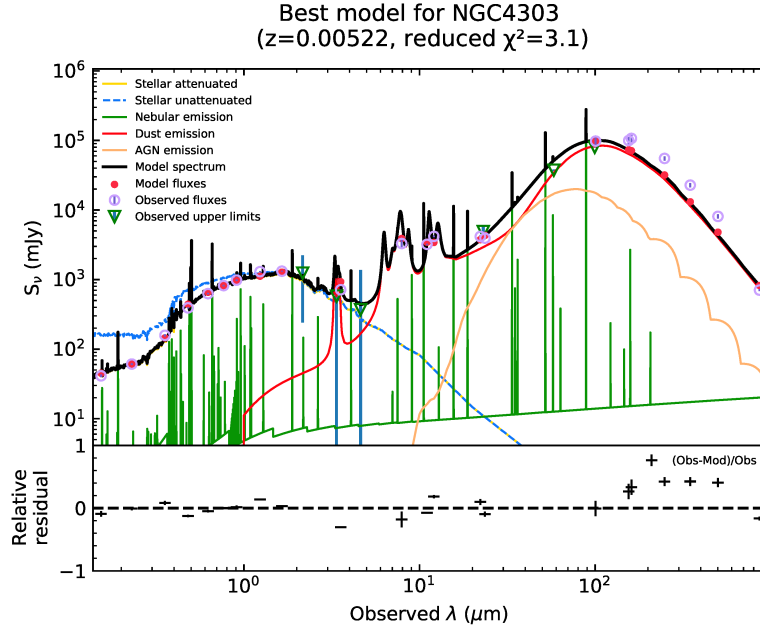
Fig. 3. The best SED model fit for NGC 4303 using CIGALE. Shown are the observed fluxes (purple circles), model fluxes (red dots), total model (black line), unattenuated stellar emission (blue line), attenuated stellar contribution (yellow line), nebular emission (green line), dust emission (red line) and AGN emission (orange line). The bottom panel shows the residuals of the observed to the model fluxes. The color figure can be viewed online.

and a common 47′ FOV. In the case of Herschel data, we used observations obtained with the Photodetector Array Camera and Spectrometer (PACS; Poglitsch et al. 2010), in the 100 μm (PACSgreen) and 160 μm (PACSred) bands with angular resolution of 8″ and 13″, respectively, and a 3′.5×1′.75 FOV, as well as the Spectral and Photometric Imaging Receiver (SPIRE; Griffin et al. 2010), in the 250 μm (PSW), 350 μm (PMW) and 500 μm (PLW) bands with angular resolutions of 18″, 25″ and 36″, and a 8′.0×4′.0 FOV. PACS data were collected from Auld et al. (2013), whereas the SPIRE data were collected from Chen et al. (2018). Finally, we used observations taken with the Submillimeter Common-User Bolometer Array (SCUBA; Holland et al. 1999) instrument on the James Clerk Maxwell Telescope (JCMT). These observations in the 850 μm band were taken from Di Francesco et al. (2008) having an angular resolution of 22″.9 and a 2′.3 FOV.

We fitted the SED of NGC 4303 using typical choices of the components to fit galaxies harbouring an AGN (e.g. Wang et al. 2020; Santos et al. 2021), a delayed star formation history with an optional exponential burst, and stellar populations model by Bruzual & Charlot (2003) using the `sfhdelayed` module with a Chabrier (2003) initial mass function (`bc03`). We considered nebular emission to account

for any Lyman continuum emission (`nebular`). The attenuation law (`dustatt_modified_starburst`) is that of Calzetti et al. (2000), whereas the dust emission was modeled using Jones et al. (2017) models (`themis`). For the AGN component we used the CLUMPY[9] models through the `nenkova2008` module, which considers the emission from a clumpy torus (Nenkova et al. 2008a,b). This latter module has recently been used successfully in other SED fitting studies of AGNs given its flexibility regarding the geometrical parameters of the torus (Miyaji et al. 2019; Yamada et al. 2023). Each of the aforementioned modules, corresponding to the physical components, has its own parameters that can take several values to form the grid of models to be fitted to the SED. The physical components, corresponding modules, parameters, and values adopted in this analysis are listed in Table 6.

In Figure 3 we present the best fit for the NGC 4303 SED. The observed fluxes (purple circles), model fluxes (red circles), and total model (black line) are shown. The different physical components used were as follows: the stellar component before (yellow line) and after attenuation (blue dashed line), dust emission (red line), nebular emission (green lines), and AGN component (ap apri-

_____

[9] `https://clumpy.org/`.

cot line). The flux residuals in each band are shown in the bottom panel and are calculated as $(S_{\nu,\mathrm{obs}} - S_{\nu,\mathrm{model}})/S_{\nu,\mathrm{obs}}$. The reduced χ^2 of the fit was 3.1.

Regarding the geometrical parameters of the clumpy dusty torus obtained with the best fit and the Bayesian analysis values (in parenthesis), we obtained a thick torus given its aperture above the equatorial plane `op_angle` = 60° (56°±9°), a large optical depth `tau_V`=200 (184±38), a large number of clouds along the equatorial plane `N_0`=15 (14±2), and an inner to outer radius ratio of `Y_ratio`=100 (97±12). The power of the radial distribution of clouds ($\propto r^{-q}$) is q=0.0 (0.12±0.29) and the viewing angle is `incl`=80° (67°±16°). Considering the classical unified AGN model (Antonucci 1993; Urry & Padovani 1995) this viewing angle is in agreement with the Sy 2 classification of Véron-Cetty & Véron (2006).

The total AGN and torus luminosities of the best fit and the Bayesian analysis values (in parenthesis) are L_{AGN} = 1.5×10^{44} erg s^{-1} [$(1.5 \pm 0.6)\times10^{44}$ erg s^{-1}], L_{TORUS} = 6.975×10^{43} erg s^{-1} [$(7.1 \pm 2.8) \times10^{43}$ erg s^{-1}], while the galaxy dust luminosity is L_{DUST} = 2.8×10^{44} erg s^{-1} [$(2.8 \pm 0.1) \times10^{44}$ erg s^{-1}], and the total IR luminosity is 3.5×10^{44} erg s^{-1} $(3.51 \pm 0.30)\times10^{44}$ erg s^{-1}. Another important quantity derived from CIGALE is the star formation rate, which in this case is $SFR = 6.014$ M$_\odot$ yr^{-1} (5.969 ± 0.298 M$_\odot$ yr^{-1}). The parameters derived from CIGALE are presented in Table 7.

5. DISCUSSION

5.1. *Dense and Diffuse Gas Masses and Kinematics*

The molecular hydrogen mass obtained for the telescope's main beam center in the ^{13}CO line can be compared with that found by Schinnerer et al. (2002) in a high spatial resolution study (≈ 150 pc) of gas traced by the ^{12}CO (J=1-0) line made with the *Owens Valley Radio Observatory* (OVRO). As can be seen in Figure 4, the molecular gas emission is found in two lanes: the western gas lane (LW) and the eastern gas lane (LE), both curving towards the nucleus (N). It was found that the central 8″ (≈ 630 pc) concentrates a mass $M(H_2) \approx 7\times10^7$ M$_\odot$. Their estimation used the conversion factor α_{CO}= 4.36 M$_\odot$ pc^{-2}(K km s^{-1})$^{-1}$ from Strong et al. (1988), with a ±30% uncertainty. In addition, the southern component of LW and the north component of LE that extend to an area of $\approx22''\times22''$, concentrate almost twice the value of the nuclear disk or central 8″ mass, see Table 3 in Schinnerer et al. (2002). Consequently this yields a total central molecular mass $M(H_2) \approx 1.81\times10^8$ M$_\odot$.
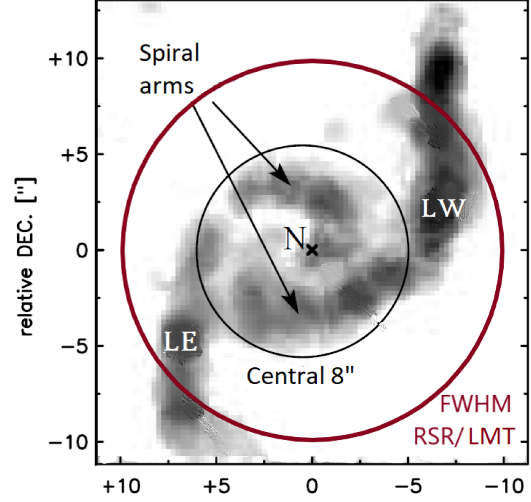

Fig. 4. A high spatial resolution ($\approx$150 pc) map of the center of NGC 4303 observed with OVRO in the ^{12}CO (1-0) line obtained by Schinnerer et al. (2002) covering $22''\times22''$. The center (black circle) has a diameter of 8″, and the red circle is an RSR/LMT region of 20″ which represents the LMT main beam for the ^{13}CO frequency. The bulk of molecular gas in this region obtained by Schinnerer et al. (2002) was compared with that obtained in our study using the ^{13}CO line. The color figure can be viewed online.

If we use instead the integrated intensity of the ^{12}CO (J=1-0) line obtained from the literature (Israel 2020), the molecular mass associated with this line derived from Σ_{mol} = 220 ± 79 M$_\odot$ pc^{-2} (see §4.1), for an area with a diameter of 22″ ($\approx$1.8 kpc) is $(5.7 \pm 2.0) \times 10^8$ M$_\odot$. Using the same conversion factor α_{CO} in both calculations, the factor of 3 difference in both masses could be due to the spatial resolution with which the observations were made, a beam of $\approx$150 pc vs. $\approx$1.8 kpc. In the second case, assuming a constant beam filling factor overestimates the amount of emission within the observed area.

In this study, the calculated molecular H_2 mass was $M(H_2)$=$(1.75\pm0.32)\times10^8$ M$_\odot$, which is in good agreement with the value reported by Schinnerer et al. (2002). We note that although the RSR/LMT observed region (the circle of 20″$\approx$1.6 kpc of diameter) does not completely cover the arms as shown in Figure 4, most of the molecular gas is concentrated in the central region, which explains the similar values. Schinnerer's work covers a slightly larger area than the one presented here, so to properly compare $M(H_2)$, we consider the value from Schinnerer et al. (2002) presented above as an upper limit.

TABLE 5

PHOTOMETRY USED IN THE SED FITTING WITH CIGALE

Band	λ_{eff} (μm)	Flux[†] (mJy)	Telescope/Instrument or Survey	Res. [††] ($''$)	FOV ($'$)	Ref.
FUV	0.153	41.3±1.9	GALEX	5.3	72.0	1
NUV	0.231	61.0±1.7	GALEX	5.3	72.0	1
u	0.352	158.0±5.0	SDSS	≤ 1.5	180.0	2
g	0.482	392.0±7.0	SDSS	≤ 1.5	180.0	2
r	0.625	628.0±12.0	SDSS	≤ 1.5	180.0	2
i	0.763	819.0±15.0	SDSS	≤ 1.5	180.0	2
z	0.902	982.0±28.0	SDSS	≤ 1.5	180.0	2
J	1.2	1300.0±20.0	2MASS	2.0	8.5	3
H	1.6	1320.0±20.0	2MASS	2.0	8.5	4
Ks	2.2	1240.0±-999.0	2MASS	2.0	8.5	5
W1	3.35	578.0±-999.0	WISE	6.1	47.0	5
IRAC1	3.6	714.0±1.0	Spitzer/IRAC	1.7	5.0	6
IRAC2	4.5	479.0±1.0	Spitzer/IRAC	1.6	5.0	6
W2	4.60	370.0±-999.0	WISE	6.4	47.0	5
IRAC4	8.0	3300.0±410.0	Spitzer/IRAC	1.9	5.2×5.2	7
W3	12	4180.0±110.0	WISE	6.5	47.0	7
IRAS1	12	3210.0±50.0	IRAS	30.0	63.6	8
W4	22	4160.0±190.0	WISE	12.0	47.0	9
MIPS24	24	3940.0±160.0	Spitzer/MIPS	6.0	5.4×5.4	10
IRAS2	25	4900.0±-999.0	IRAS	30.0	63.6	11
IRAS3	60	37300.0±-999.0	IRAS	60.0	63.6	11
PACSgreen	100	97900.0±11800.0	Herschel/PACS	8.0	3.5×1.75	12
IRAS4	100	79700.0±-999.0	IRAS	120.0	63.6	13
MIPS160	160	99800.0±12000.0	Spitzer/MIPS	38.0	2.1×5.3	10
PACSred	160	107000.0±13000.0	Herschel/PACS	13.0	3.5×1.75	12
PWS	250	55200.0±3900.0	Herschel/SPIRE	18.0	8.0×4.0	14
PWM	350	22800.0±1600.0	Herschel/SPIRE	25.0	8.0×4.0	14
PWL	500	8100.0±580.0	Herschel/SPIRE	36.0	8.0×4.0	14
SCUBA2	850	705.0±20.0	JCMT/SCUBA	22.9	2.3	15

REFERENCES: (1) Cortese et al. (2012); (2) Kim et al. (2014); (3) Bai et al. (2015); (4) Dalya et al. (2016); (5) Stassun (2019): (6) Sheth et al. (2010); (7) Ciesla et al. (2014); (8) Moustakas & Kennicutt (2006); (9) Boselli et al. (2014); (10) Bendo et al. (2012); (11) Rahman et al. (2006); (12) Auld et al. (2013); (13) Yun et al. (2001); (14) Chen et al. (2018); (15) Di Francesco et al. (2008).

[†] The flux data without error estimates (-999.0) are taken as upper limits in the SED fitting analysis (green upside down triangles in Figure 3).

[††] Telescope resolution.

As we saw in the previous section, the $M(H_2)$ value obtained with ^{12}CO and equation (7) is three times the value obtained with ^{13}CO. This difference may be due to the conversion factor α_{CO}, although in many studies it is assumed to be a constant value across various scales, and environments, recent studies have found variations of 1-2 orders of magnitude that depend on the physical properties of the medium. Teng et al. (2023) observed the central ≈ 2 kpc region of two barred spiral galaxies at ≈ 100 pc resolution with ^{12}CO and found a correlation between α_{CO} and the optical depth, an anticorrelation with kinetic temperature of the gas and low values of α_{CO} by factors of 4-15 in the central regions of these galaxies. As we can see, this variation has a significant impact on the calculation of molecular

TABLE 6

PARAMETERS USED IN THE SED FITTING WITH CIGALE

Component	Module	Parameter	Values
SFH	sfhdelayed	tau_main	1000, 2000, 4000, 6000 (Myr)
		age_main	1500, 4000, 8000 (Myr)
		tau_burst	10, 25 (Myr)
		age_burst	10, 20 (Myr)
		f_burst	0.0, 0.01
Stellar emission	bc03	imf	Chabrier (2003)
		metallicity	0.0001, 0.0004, 0.004, 0.008, 0.02, 0.05
		separation_age	10 (Myr)
Nebular emission	nebular	logU	-2.0
		f_esc	0.0
		f_dust	0.0
		lines_width	300.0
Attenuation	dustatt_modified	E_BV_lines	0.0, 0.3, 0.6, 0.9, 1.2, 1.5, 1.8, 2.1, 2.4
law	_starburst	E_BV_factor	0.44
		uv_bump_wavelength	217.5
		uv_bump_width	35.0
		uv_bump_amplitude	0, 1.5, 3
		powerlaw_slope	-0.2, 0
		Ext_law_emission_lines	1 (MW)
		Rv	3.1
Dust emission	themis	qhac	0.06, 0.17, 0.36
		umin	0.1, 1.0, 10.0, 50.0
		alpha	1.0, 2.0, 3.0
		gamma	0.1, 0.25
AGN	nenkova2008	Y_ratio	5, 10, 30, 60, 100
		op_angle	20, 40, 60
		tau_V	20, 60, 80, 120, 200
		N_0	3, 5, 10, 15
		incl	10, 30, 60, 80
		q	0.0, 0.5, 1.0, 2.0, 3.0
		fracAGN	0.0, 0.1, 0.2, 0.3, 0.4, 0.5, 0.6, 0.7, 0.8, 0.9

masses and the quantities derived from it, so care must be taken in choosing the value of α_{CO} according to the scale and characteristics of the ISM. In this paper, we consider the value of $M(H_2)$ obtained with ^{13}CO to be the most accurate.

The surface density of dense molecular gas (Σ_{dense}) obtained using equation (8) is integrated in a region where the molecular gas is not homogeneously distributed and thus Σ_{dense} may be underestimated (see Figure 4). An important result is the calculation of the amount of dense gas traced by the HCN in the same region $M_{dense} = (4.7 \pm 0.3) \times 10^7 \, M_\odot$. This value resulted ≈ 4 times smaller than the total mass of molecular hydrogen. This dense star-forming gas provides the conditions for the 200–250 pc diameter circumnuclear ring studied by Riffel et al. (2016), through observations in the UV-optical-IR; they reveal intense bursts of star formation. The relationship between dense and molecular mass is $M_{dense}=0.21 \, M(H_2)$ which is comparable to $f_{dense}= 0.13\pm0.06$, within the uncertainties.

TABLE 7

AGN AND DUSTY TORUS PROPERTIES
AFTER SED FITTING WITH CIGALE

Parameter	Best Fit Result	Bayessian Analysis
Y_ratio	100	97 ± 12
op_angle($^\circ$)	60	56 ± 9
tau_V	200	184 ± 38
N_0	15	14 ± 2
incl($^\circ$)	80	67 ± 16
q	0.0	0.12 ± 0.29
fracAGN	0.2	0.20 ± 0.07
SFR (M$_\odot$ yr^{-1})	6.0	6.0 ± 0.3
L_{AGN} (erg s^{-1})	1.5×10^{44}	$(1.5 \pm 0.6)\times10^{44}$
L_{TORUS} (erg s^{-1})	7.0×10^{43}	$(7.1 \pm 2.8)\times10^{43}$
L_{DUST} (erg s^{-1})	2.8×10^{44}	$(2.8 \pm 0.1)\times10^{44}$
$L_{IR} =$ (erg s^{-1})	3.5×10^{44}	$(3.51 \pm 0.30)\times10^{44}$

Regarding gas kinematics, we analyzed the velocity of the molecular emission lines and compared them with those of previous studies. The rotational curve of the galaxy traced by molecular gas ^{12}CO J=(2-1) with a resolution of $\approx$150 pc from ALMA observations (Figure D3, Lang et al. 2020) shows the fitting of the observational data, resulting in an asymptotic rotation velocity $V_0 = 178.2^{+75.1}_{-43.0}$ km s^{-1}. Meanwhile, the curves obtained by simulations of a central bar formation made by Iles et al. (2022), show that, for an $r \leq 2$ kpc radius, the rotational velocity V_{rot} from the simulations (IsoB IC, blue curves in Figure A1 in that paper) is in the range of 150 to 175 km s^{-1}.

In this study, the velocities for the diffuse gas, i.e., ^{13}CO and C^{18}O, gave us a mean velocity of $V_{CO} = 151 \pm 29$ km s^{-1} that matches with the rotational velocity in the $r \leq 2$ kpc radii obtained by Iles et al. (2022), i.e., which covers partially the bar radius $r_{bar} = 2.50 \pm 0.63$ kpc (e.g., Zurita et al. 2021); this is important because in this region the bar dominates the gas kinematics. Meanwhile, the mean value of the velocity for dense gas tracers HCN, HNC, and HCO$^+$ is $V_{dense} = 178 \pm 60$ km s^{-1}, which is consistent with the results obtained by Lang et al. (2020). The dense gas velocity is comparable to the diffuse gas, even having different FOVs. This is maybe due to the dominance of the structural component of the bar.

5.2. Emission Line Ratios

The molecular emission line ratio method helps to quantify the molecular gas in specific regions of the galaxy, as in the case of AGN, and can pro-

vide information to characterize the star formation or SMBH accretion processes. In this work, we are trying to determine if the presence of the AGN is hinted at by the line ratios and to characterize the ISM from this central 1.6 kpc region.

Previous studies have attempted to classify the activity of galaxies using molecular emission line diagrams such as HNC/HCN, or highest values of HCN/HCO$^+$ (Kohno et al. 2001; Costagliola et al. 2011; Jiang et al. 2011).

Another example is the use of the HNC/HCN ratio as an indicator of shock and non-standard heating, or the CS/HCN ratio, which should be greater than one at large column densities for both XDRs and PDRs, suggesting a correlation with column density (Baan et al. 2008).

Jiménez-Donaire et al. (2019) studied dense gas in nine nearby galaxies at $\approx$1-2 kpc resolution and showed that the main emission line ratios had a maximum value at the center (with radius ≈ 0.8 kpc) and decreased radially towards the outermost parts of the disk or spiral arms. Using values from Jiménez-Donaire et al. (2019) and our study, we present in Figure 5 the diagnostic diagram of HNC, HCN, HCO$^+$ relative to ^{12}CO. We observe an increasing relationship that clearly separate the galaxy regions, with the galactic centers being the most intense. The ratios HCN/^{12}CO, HCO$^+$/^{12}CO and HNC/^{12}CO presented in Table 4 for the center of NGC 4303 are located in the diagnostic diagram as mentioned previously. As shown, our values are located in the region where the galactic central regions are also located. It should be noted that the center of the galaxy closest to our point is the barred spiral galaxy NGC 6946, which is also classified as a Sy 2.

The ratio between ^{12}CO and ^{13}CO is denoted by $R_{12/13}$ and has been studied for a large sample of galaxies because these lines are generally more intense and easier to detect (e.g., Aladro et al. 2015; Israel 2020). The value $R_{12/13}$ for the nucleus of the galaxy NGC 4303 is 12.1 ± 1.4, consistent with the mean value $R_{12/13} = 13 \pm 6$ of nearby starburst galaxies found by Aalto et al. (1995). This ratio provides information on the variation in optical depth in each galaxy, as well as on the relative abundances of ^{12}C and ^{13}C. In the case of ^{12}C, this can be produced by supernovas of massive stars, whereas ^{13}C can be produced in low-mass stars or ion exchange ^{13}C$^+$ in regions with temperatures ≈ 10 K (see, for example, Keene et al. 1998; Davis 2014).

The HNC/HCN $= 0.58 \pm 0.04$ ratio shows that the HNC abundance is lower than that of HCN. Hirota et al. (1998) observed 19 nearby dark cloud

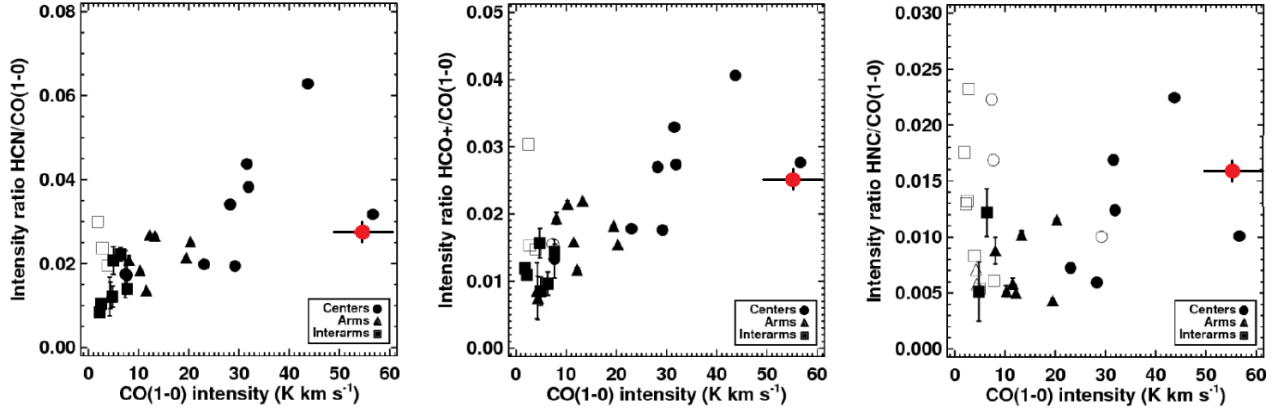Fig. 5. Diagnostic diagrams left-to-right HCN/^{12}CO, HCO$^+$/^{12}CO and HNC/^{12}CO for a sample of nine nearby galaxies from Jiménez-Donaire et al. (2019). Squares are the values in the interarm regions, triangles are the values in the arms and circles are the values in the centers of these galaxies. Open symbols represent upper limits. The red circles represent the values for the central region of NGC 4303 obtained in this study, which is consistent with the location of the centers of other spiral galaxies on the diagram. The color figure can be viewed online.

cores with Nobeyama 45 m. According to them, the HNC/HCN value is a consequence of the temperature of the central molecular region, $T_{ex} > 24$ K, where neutral-neutral reactions occur. In this manner, the HNC molecule is destroyed to form its isomer, HCN. This supports the use of $T_{ex} = 30$ K to derive surface densities with the corresponding value of $M(H_2)$.

HCN/HCO$^+$ is the ratio most sensitive to density changes, because the critical density of HCO$^+$ is one order of magnitude smaller than that of HCN. Therefore, HCO$^+$ tends to recombine faster than HCN when the medium is dense, owing to free electrons. However, both molecules have similar abundances, indicating that at high densities there is a possible mechanism that enhances the abundance of HCO$^+$. Studies of molecular abundance by Meijerink & Spaans (2005) suggest that, in PDRs, this molecule abundance enhancement occurs at densities $n > 10^5$ cm^{-3}. As mentioned previously, HCN/HCO$^+$ has also been used to determine the nature of the nuclear emitting source. In particular, values of HCN/HCO$^+$ greater than one were found in XDRs, caused by AGN with low density $n > 10^4$ cm^{-3} and $N(H_2) < 10^{22}$ cm^{-2} (for example, Loenen et al. 2008), which agrees with the values of HCN/HCO$^+$ = 1.10 and $N(H_2)$ found in our study (see Table 2). Recently, Nishimura et al. (2024) found in a sample of 23 local ULIRGs that this ratio (J=3-2 lines) shows no trend with AGN luminosity and no implication in the SFR, but the presence of outflows or inflows has the most crucial influence. The HCN/HCO$^+$ ratio indicates a very

similar abundance between the two molecules. Thus, HCO$^+$ can form in the dense region, that is, when $n_{critic} > 10^5$ cm^{-3}, ionization must occur in the medium through shock waves or PDRs produced by young stars. The stellar populations of the circumnuclear region described by Dametto et al. (2019) are young ($t < 2$ Gyr) and add a high density to the medium, reinforcing the idea that the gas in the region has high ionization probabilities for radical formation.

Recently, Neumann et al. (2023) presented the results of the ALMOND (ACA Large-sample Mapping Of Nearby galaxies in Dense gas) survey, where they traced the molecular gas density using resolved measurements of HCN(1-0) across 25 nearby spiral galaxies, one of which was NGC 4303. The HCN beam in that work ($20'' \approx 1.6$ kpc) is similar to ours, and therefore the results can be compared. The HCN integrated intensity in the 2 kpc galactocentric radius has a peak temperature of 9.4 mK, similar to our value (see Table 1). In the upper left panel of Figure 6 of Neumann et al. (2023), the relationship between HCN(1-0)/^{12}CO(2-1) and (Σ_{mol}) is presented; our logarithmic values are -1.55 and 2.05, respectively, which lie on their linear relation. This data point is within the range of values for log HCN/^{12}CO reported for NGC 4303 (see their Figure I4). Our Σ_{mol} is in the lower end of the range reported in Neumann et al. (2023), but we note that their value was calculated as a cloud-scale property at 150 pc resolution using α_{CO}, whose uncertainty can be attributed to variations in the galactocentric radius (e.g., Sandstrom et al. 2013).
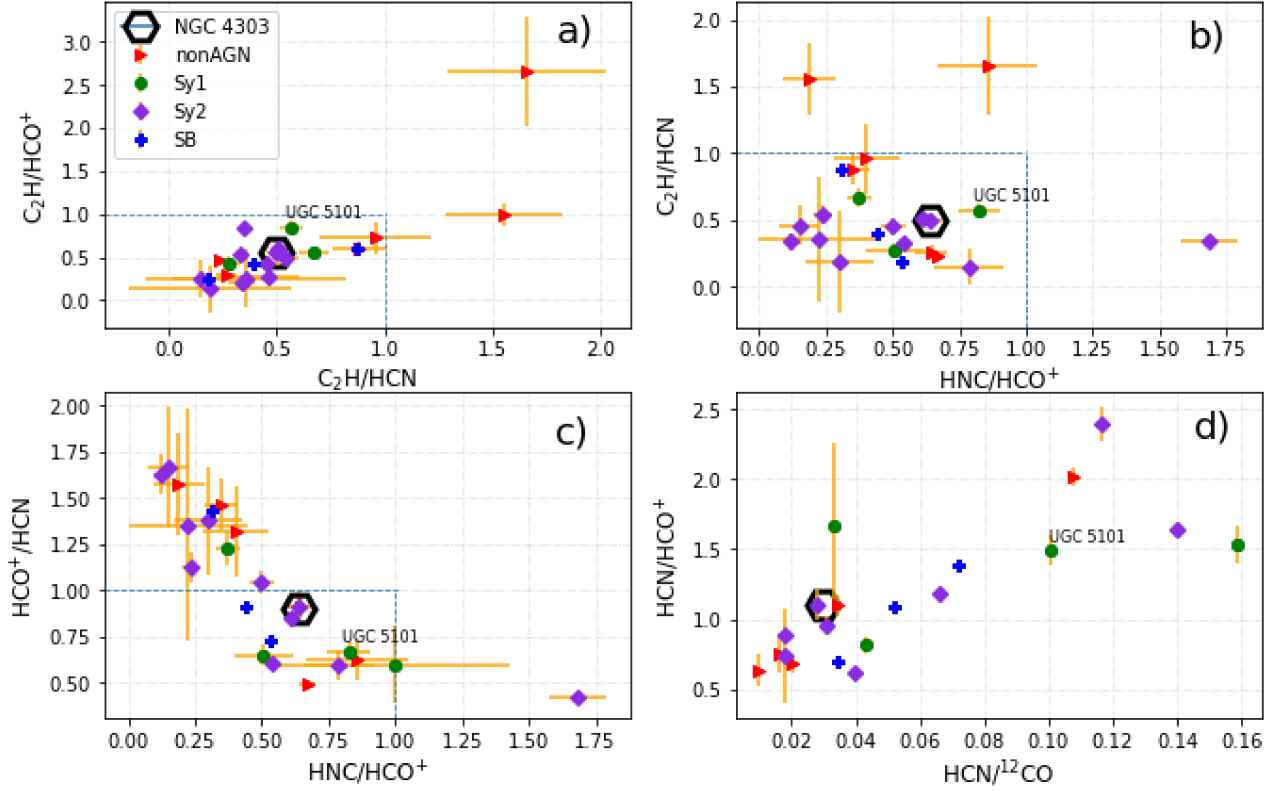
Fig. 6. Line ratio diagrams for a set of 22 galaxies in the literature plus the central 1.6 kpc of NGC 4303. Left to right: a) C_2H/HCN vs. C_2H/HCO^+, b) HNC/HCO^+ vs. C_2H/HCN, c) HNC/HCO^+ vs. HCO^+/HCN, d) $HCN/^{12}CO$ vs. HCN/HCO^+. The line ratio values from the literature are integrated values, the open black hexagons are the values for the central 1.6 kpc of NGC 4303. In addition, the values for UGC 5101 obtained by Cruz-González et al. (2020) in a similar study are labeled in each diagram. The dashed blue line encloses the region where the ratio is less than one. The color figure can be viewed online.

Diagnostic diagrams were constructed to determine possible relationships between type of galaxy activity and emission lines. In Table 8 we present a sample of 23 normal main sequence, starburst (SB), AGN Sy 1 and AGN Sy 2 galaxies with integrated intensities of HCN, HNC, C_2H, HCO^+, ^{12}CO and ^{13}CO reported in the literature. The sample is displayed in Figure 6, and includes the values for the central region of NGC 4303 as a black circle. In these diagrams no relationship between the line intensity ratios and galaxy activity is observed, the SB types and AGNs are mixed, and NGC 4303 lies between the groups. Linearity trends can be observed between the ratios: C_2H/HCN vs. C_2H/HCO^+, HNC/HCO^+ vs. HCO^+/HCN and $HCN/^{12}CO$ vs. HCN/HCO^+.

In the first relation, (a) in Figure 6, we can see a linear relation between these ratios; also, the majority of the galaxies lie in the region where the ratios are less than one, with the special cases of

NGC 3556 and IC 180. The diagram (d) $HCN/^{12}CO$ vs. HCN/HCO^+ shows an increasing relation too, where, for values of HCN/HCO^+ less than one, most of the galaxies have a low fraction of dense gas ($\lesssim 0.05$) and for values greater than one the amount of dense gas, with respect to diffuse gas, grows by a factor of 5-8. This last point may indicate a strong relationship between HCO^+ and CO. Additionally, having a dense gas fraction greater than 5% may be linked to the recombination of HCO^+ and increase the abundance of HCN molecules.

The presence of C_2H in the central region may be associated with reactions produced by PDRs in massive, hot star formation regions (for example, Martín, S. et al. 2015). This molecule, like other simple hydrocarbons (^{13}CN, CH, c-C_3-H_2) is the product of keeping a large amount of carbon ionized with warm gas associated with ultraviolet radiation, therefore, the intensity of the field is proportional to its abundance (Meier & Turner 2005; Meier et al. 2015). It

TABLE 8

MOLECULAR LINE TRANSITIONS DETECTED IN NGC 4303 AND OTHER GALAXIES

Galaxy	$\dfrac{C_2H}{HCO^+}$	$\dfrac{C_2H}{HCN}$	$\dfrac{HCN}{HCO^+}$	$\dfrac{HNC}{HCO^+}$	$\dfrac{HCN}{^{12}CO}$	Activity[*]	Reference[**]
NGC 4303	0.55	0.50	1.10	0.64	0.03	Sy2	a
UGC 5101	0.84	0.56	1.50	0.83	0.10	Sy1.5	b
IC 180	2.65	1.66	1.60	0.86	-	-	c
NGC 1614	0.26	0.54	0.74	0.22	0.02	Sy2	c
NGC 3079	0.48	0.54	0.89	0.24	0.02	Sy2	c
NGC 4194	0.73	0.96	0.76	0.40	0.02	-	c
NGC 4388	0.14	0.19	0.73	0.30	-	Sy2	c
NGC 4418	0.25	0.15	1.69	0.79	-	Sy2	c
NGC 6090	0.27	0.46	0.60	0.15	-	Sy2	c
NGC 6240	0.21	0.34	0.61	0.12	0.04	Sy2	c
NGC 7771	0.29	0.26	1.10	0.65	0.03	-	c
NGC 660	0.43	0.45	0.96	0.50	0.03	Sy2	c
NGC 3556	0.99	1.56	0.64	0.19	0.01	-	d
NGC 2273	-	-	1.67	1.00	0.03	Sy1-2	d
NGC 5236	0.43	0.39	1.09	0.44	0.05	SB	e
NGC 253	0.60	0.51	1.18	0.61	0.07	Sy2	e
M82	0.61	0.87	0.70	0.31	0.03	SB	e
M51	0.47	0.23	2.02	0.67	0.11	-	e
NGC 1068	0.54	0.33	1.64	0.54	0.14	Sy2	e
NGC 7469	0.55	0.67	0.82	0.37	0.04	Sy1.2	e
ARP 220	0.83	0.35	2.39	1.68	0.12	Sy2	e
MRK 231	0.43	0.28	1.54	0.51	0.16	Sy1	e
IC 342	0.25	0.18	1.38	0.54	0.07	SB	f

Notes: [*]Activity type from NASA/IPAC Extragalactic Database (NED).
[**]Dense gas emission line ratios from: [a]This work, [b]Cruz-González et al. (2020), [c]Jiang et al. (2011), [d]Costagliola et al. (2011), [e]Aladro et al. (2015), [f]Nakajima et al. (2018).

is worth noting that we have possible detections of some hydrocarbons that reinforce the idea of the presence of these PDRs.

In Figure 7 we show $R_{12/13}$ vs. HCO$^+$/HCN. We can observe another increasing relation, where the galaxies with values of HCO$^+$/HCN less than one have values of $R_{12/13} < 15$, that is, close to the mean value for nearby starburst galaxies found by Aalto et al. (1995). Note that this ratio is an indicator of the optical depth of the gas, that is, when $R_{12/13}$ increases, the medium becomes optically thicker. Therefore, HCO$^+$/HCN could be a possible indicator of highly obscured galaxies.

As described above, the integrated molecular gas diagrams cannot offer a diagnosis of the presence or absence of obscured AGNs, as the Sy 1 and Sy 2 galaxies show no differences. However, they can tell us more about the abundance of the molecular gas in terms of the change in density and temperature conditions in the regions near the galactic centers. This can lead to a characterization of the conditions of active star formation or its suppression in the regions surrounding an SMBH.

Separating the contribution of the central AGN from the rest of the galaxy is a problem. Observationally, the telescope's main beam is usually larger than the galaxy diameter; hence, the intensity of the lines usually includes contribution of arms (disk) and the bar (if any). In addition to this spatial resolution problem, it is important to detect high transitions of dense gas tracers with the disadvantage that they are even weaker in intensity than those of the rotational transition J=(1-0), when they are optically thin. An example of such a study is reported in Imanishi et al. (2023), a study with ALMA $\lesssim$0.5 kpc resolution, where they detected the J=2-1, J=3-2 and J=4-3 high transition of several emission lines in 11 ULIRGs and showed the spatial variations of physical and chemical properties of molecular gas within the $\lesssim$2 kpc nuclear regions.
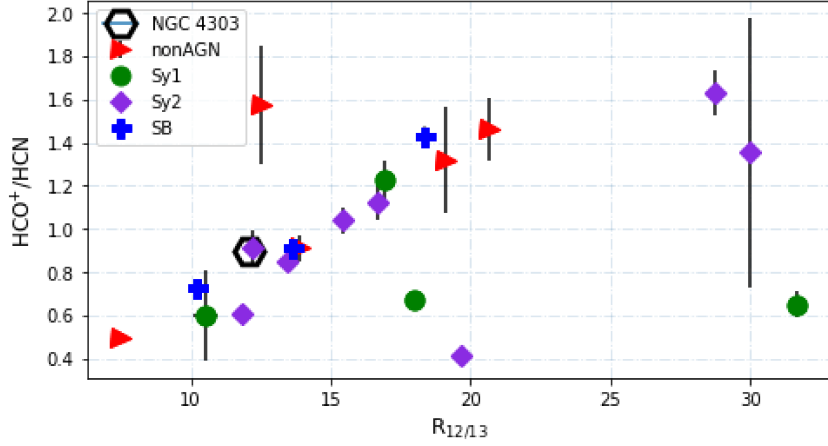
Fig. 7. $R_{12/13}$ vs. HCO$^+$/HCN for a sample of 12 nearby galaxies. The open black hexagon is the value for the center of NGC 4303. Although a clear linear dependence can be seen between the lines, there is no dependence on galactic activity. The color figure can be viewed online.

5.3. L_{HCN} vs. L_{IR} Relation

One of the outcomes of the SED fitting analysis is the total infrared luminosity L_{IR}, which is estimated as the sum of the torus luminosity L_{TORUS}, and the dust luminosity, L_{DUST}. From the Bayesian analysis values we obtained $\log(L_{IR}) = 10.96 \pm 0.04\, L_\odot$ (see Table 7). Sanders et al. (2003) reported a similar value $\log(L_{IR}) = 10.51\, L_\odot$ for NGC 4303, determined using the fluxes in all four IRAS bands. Both L_{IR} values were larger than those of Li et al. (2020), who reported $\log(L_{IR}) = 9.6 \pm 0.03\, L_\odot$. However, Li et al. (2020) processed calibrated IR image data from Spitzer MIPS and Herschel PACS instruments and corrected to the IRAM telescope main beam (which is close in size to the main beam of the LMT), to estimate L_{IR}. For that reason, we use the value of $\log(L_{IR})$ from Li et al. (2020), together with our derived value for $\log(L_{HCN}) = 6.87 \pm 0.08$ K km s^{-1} pc^2 (Table 3) to place NGC 4303 in Figure 2 of Bigiel et al. (2016) and Figure 5 of Neumann et al. (2023). In both cases, NGC 4303 lies close to the star formation sequence of a sample of nearby galaxies and individual molecular cloud cores, in the group of active star-forming disk galaxies. As we can see, the L_{HCN} vs. L_{IR} relation presented by Neumann et al. (2023) is independent of disc, arm or interarm regions in spatially resolved galaxies.

From a similar analysis for the galaxy UGC 5101 presented by Cruz-González et al. (2020), which was observed in the same season with the RSR/LTM, we obtain $\log(L_{HCN}) = 8.87 \pm 0.02$ K km s^{-1} pc^2 and taking $\log(L_{IR}) = 11.81 \pm 0.08\, L_\odot$ from Soifer et al. (1989), this object falls among the luminous infrared galaxies (LIRGs) in the correlation from Bigiel et al. (2016).

5.4. AGN Component and SFR in NGC 4303 from SED Fitting

According to the results of the SED fitting (see Table 7), the AGN component in NGC 4303 is rather low, with an AGN fraction value (`fracAGN`) of 0.2. Indeed, other studies that use CIGALE to fit AGN components to SEDs of galaxies have analyzed its reliability in determining the AGN contribution compared with optical classification and color-color diagrams (for example, Wang et al. 2020) and found a minimum value of `fracAGN` = 0.2 as a reliable lower limit for classifying AGNs using this method. Thus, the value of `fracAGN` that we find allows us to classify NGC 4303 at least as a marginally AGN, and could be in agreement with the difficulties to classify this galaxy as centrally dominated by star formation or a SMBH, and perhaps is speaking in favor of the fading phase AGN scenario (Esparza-Arredondo et al. 2020).

To asses the goodness of the fit and to validate the properties derived from it, we look at the value of the reduced χ^2, which in our case is 3.1. We consider that this value corresponds to a fairly good fit and confirm this by visual inspection (see Figure 3). We notice, however, that the residuals at far-infrared wavelengths are higher than those at both, shorter and longer (sub mm) wavelengths, but the model fluxes (red dots) still describe the shape of the observations. This could be caused by the fact that the observation at 100μm, just before the region of the higher residuals, is very well described by the model

(residual ≈ 0), hence pinning the model at that point and preventing it from describing the far-infrared observations in a better manner.

Regarding the SFR in NGC 4303, previous works have reported its estimated value using UV and infrared maps. Utomo et al. (2018) estimated the SFR from the combined GALEX FUV map, corrected for galactic extinction, and the WISE W4 infrared map. The maps were convolved to have an angular resolution of 15″ and background subtracted. After this, they applied the prescriptions described in Kennicutt & Evans (2012) and Jarrett et al. (2013), obtaining a SFR=5.24 $M_\odot$ yr^{-1}. A similar analysis was done by Chevance et al. (2020) in a FOV of roughly the size of the galaxy (see their Figure 1), obtaining a SFR=4.37 $\pm$ 0.87 $M_\odot$ yr^{-1}. Leroy et al. (2019) calibrated the above mentioned prescriptions to match the results from Salim et al. (2016, 2018) who combined GALEX, WISE and SDSS data to estimate the integrated SFR for low-redshift galaxies using CIGALE. The value they found is SFR=5.49$\pm$1.58 $M_\odot$ yr^{-1}. More recently, Leroy et al. (2021) adopted the prescription of Leroy et al. (2019) using a linear combination of FUV and W4 light, converting the luminosity of each band to SFR using the respective conversion factors and adding the UV and infrared terms to obtain the value SFR=5.37 $M_\odot$ yr^{-1}.

In summary, previous values of the SFR are similar to our CIGALE value, SFR=6.0$\pm$0.3, but most authors quote somewhat smaller values. We note that our analysis has the advantage that it incorporates UV to mm wavelength photometry, and the clumpy torus component. Assuming that the values of SFR from the literature are the true values, our similar result validates the good quality of our CIGALE fit and the derived properties. Furthermore, using SFR and $M_\star$ from (Leroy et al. 2021) we note that NGC 4303 lies along the star-formation main sequence (see for example, Cano-Díaz et al. 2019, for MaNGA SDSS-IV), for nearby galaxies.

6. CONCLUSIONS

With the aim of studying the molecular gas in the obscured core of the galaxy NGC 4303, in this work we analyze the emission line spectrum obtained with the *Redshift Search Receiver* at the Large Millimeter Telescope (in its initial phase of 32 m) in the band of 3 mm (73 - 110 GHz), which correspond to 1.6 kpc centered on the ^{13}CO (110.20 GHz) line.

We detected six molecular lines with S/N>3 in the J=(1-0) rotational transition: C$_2$H (87.31 GHz), HCN (88.63 GHz), HCO$^+$ (89.18 GHz), HNC

(90.66 GHz), C^{18}O (109.78 GHz) and ^{13}CO (110.20 GHz). The first four lines are gas with critical densities $n_{critic} > 10^4$ cm^{-3} which makes them ideal for the study of dense gas that is directly responsible for star formation in the galaxy. The average velocities obtained from the Gaussian fit were 151 $\pm$ 29 km s^{-1} for the diffuse gas, and 178 $\pm$ 60 km s^{-1} for the dense gas. The result for the diffuse gas velocity is in agreement with the result of Iles et al. (2022), as well with that in the observed ^{12}CO J=(2-1) rotation curve of Lang et al. (2020).

The isotopic varieties of carbon monoxide C^{18}O and ^{13}CO trace the diffuse molecular gas with $n_{critic} \approx 10^3$ cm^{-3} and taking advantage of the fact that the ^{13}CO line is optically thin, that is, $\tau_{13} = 0.09 \pm 0.01$, the column densities relative to ^{12}CO and H$_2$ for three excitation temperatures (10, 20 and 30 K) were calculated. The results obtained with $T_{ex} = 30$ K are $N(H_2) = (5.14 \pm 0.94) \times 10^{21}$ cm^{-2} and $M(H_2) = (1.75 \pm 0.32) \times 10^8$ M$_\odot$, in good agreement with the expected theory and with results obtained by other methods. For example, the last result for the mass of molecular hydrogen is of the same order of magnitude as that found for a central region of 22″$\times$22″using a ^{12}CO(1-0) high resolution map obtained by Schinnerer et al. (2002). Using the HCN integrated intensity it was possible to calculate the amount of dense gas in the observed area. The value $M_{dense} = (4.7 \pm 0.3) \times 10^7$ M$_\odot$ is only 4 times smaller than the amount of gas in H$_2$.

The intensities of the emission lines of the dense and diffuse molecular gas tracers clearly show that the abundance with which these species enrich the chemistry of the medium is due to certain star formation activity in the circumnuclear region. PDRs are a consequence of the interaction of young stars or regions of star formation and are responsible for generating this abundance of radicals in a very dense region that would cause them to recombine quickly. The accretion mechanisms of this gas towards the center responsible for such density must be linked to both the spiral arms and the bar that reach the circumnuclear region, which may be influenced by the gravitational potential of the SMBH. Meanwhile, when comparing the line ratios obtained here with those of a sample of galaxies in the literature, no clear trend is observed to distinguish nuclear activity (SF or AGN) from normal galaxies.

Our spectral energy distribution analysis using the CIGALE code shows that NGC 4303 has a large clumpy dusty torus, with the following parameters obtained based on the Bayesian analysis: aperture

above the equatorial plane `sigma` = $56°\pm9°$, dust optical depth `tau_V`=184 ± 38, number of dust clouds along the equatorial plane `N_0`=14 ± 2, an inner to outer radius ratio of `Y_ratio`=97 ± 12, and a viewing angle of `incl`$\approx70°$. By considering the classical unified AGN model (Antonucci 1993; Urry & Padovani 1995); this viewing angle is in agreement with the Sy 2 classification previously given by Véron-Cetty & Véron (2006).

Furthermore, for NGC 4303 CIGALE yields the total AGN and torus luminosities of $L_{AGN} = (1.5\pm0.6) \times10^{44}$ erg s^{-1}, $L_{TORUS} = (7.1\pm2.8)\times10^{43}$ erg s^{-1}; while the galaxy dust luminosity is $L_{DUST} = (2.8\pm0.1) \times10^{44}$ erg s^{-1}, which yield a total infrared luminosity $L_{IR} = (3.51\pm0.30) \times10^{44}$ erg s^{-1}. Finally, the star formation rate obtained is SFR=6.0 ± 0.3 M$_\odot$/yr, which, together with the total stellar mass, places this galaxy along the star-formation main-sequence for normal nearby galaxies.

From the molecular gas and dusty torus analysis, we conclude that the central 1.6 kpc emission from NGC 4303 is a mixture of an AGN with a marginal contribution of $\leq20\%$, most probably a Type 2, with a large clumpy dusty torus and a starburst host galaxy, as evidenced by intense dense molecular gas lines (C_2H, HCN, HCO$^+$, and HNC). We found that dense gas contributed significantly to the total molecular gas mass.

REFERENCES

Aalto, S., Booth, R. S., Black, J. H., & Johansson, L. E. B. 1995, A&A, 300, 369

Abazajian, K. N., Adelman-McCarthy, J. K., Agüeros, M. A., & et al. 2009, ApJS, 182, 543, https://doi.org/10.1088/0067-0049/182/2/543

Aladro, R., Martín, S., Riquelme, D., & et al. 2015, A&A, 579, 101, https://doi.org/10.1051/0004-6361/201424918

Antonucci, R. 1993, ARA&A, 31, 473, https://doi.org/10.1146/annurev.aa.31.090193.002353

Auld, R., Bianchi, S., Smith, & et al. 2013, MNRAS, 428, 1880, https://doi.org/10.1093/mnras/sts125

Baan, W. A., Henkel, C., Loenen, A. F., Baudry, A., & Wiklind, T. 2008, A&A, 477, 747, https://doi.org/10.1051/0004-6361:20077203

Bai, Y., Zou, H., Liu, J., & Wang, S. 2015, ApJS, 220, 6, https://doi.org/10.1088/0067-0049/220/1/6

Bendo, G. J., Galliano, F., & Madden, S. C. 2012, MNRAS, 423, 197, https://doi.org/10.1111/j.1365-2966.2012.20784.x

Bennett, C. L., Larson, D., Weiland, J. L., & Hinshaw, G. 2014, ApJ, 794, 135, https://doi.org/10.1088/0004-637X/794/2/135

Bigiel, F., Leroy, A., Walter, F., et al. 2008, AJ, 136, 2846, https://doi.org/10.1088/0004-6256/136/6/2846

Bigiel, F., Leroy, A. K., Jiménez-Donaire, M. J., & et al. 2016, 2016, ApJ, 822, 26, https://doi.org/10.3847/2041-8205/822/2/L26

Bolatto, A. D., Wolfire, M., & Leroy, A. K. 2013, ARA&A, 51, 207, https://doi.org/10.1146/annurev-astro-082812-140944

Boquien, M., Burgarella, D., Roehlly, Y., et al. 2019, A&A, 622, 103, https://doi.org/10.1051/0004-6361/201834156

Boselli, A., Voyer, E., Boissier, S., & et al. 2014, A&A, 570, 69, https://doi.org/10.1051/0004-6361/201424419

Bruzual, G. & Charlot, S. 2003, MNRAS, 344, 1000, https://doi.org/10.1046/j.1365-8711.2003.06897.x

Calzetti, D., Armus, L., Bohlin, R. C., & et al. 2000, ApJ, 533, 682, https://doi.org/10.1086/308692

Cano-Díaz, M., Ávila-Reese, V., Sánchez, S. F., & et al. 2019, MNRAS, 488, 3929, https://doi.org/10.1093/mnras/stz1894

Chabrier, G. 2003, PASP, 115, 763, https://doi.org/10.1086/376392

Chen, P. S., Yang, X. H., Liu, J. Y., & Shan, H. G. 2018, AJ, 155, 17, https://doi.org/10.3847/1538-3881/aa988c

Chevance, M., Kruijssen, J. M. D., Hygate, & et al. 2020, MNRAS, 493, 2872, `https://doi.org/10.1093/mnras/stz3525`

Ciesla, L., Boquien, M., Boselli, A., & et al. 2014, A&A, 565 128, `https://doi.org/10.1051/0004-6361/201323248`

Ciesla, L., Charmandaris, V., Georgakakis, A., & et al. 2015, A&A, 576, 10, `https://doi.org/10.1051/0004-6361/201425252`

Colina, L., Piqueras López, J., Arribas, S., Riffel, R., Riffel, R. A., & et al. 2015, A&A, 578, 48, `https://doi.org/10.1051/0004-6361/201425567`

Cortese, L., Boissier, S., Boselli, A., & et al. 2012, A&A, 544, 101, `https://doi.org/10.1051/0004-6361/201219312`

Costagliola, F., Aalto, S., Rodriguez, M. I., & et al. 2011, A&A, 528, 30, `https://doi.org/10.1051/0004-6361/201015628`

Cruz-González, I., Gómez-Ruiz, A. I., Caldú-Primo, A., et al. 2020, MNRAS, 499, 2042, `https://doi.org/10.1093/mnras/staa2949`

Cybulski, R., Yun, M. S., Erickson, N., & et al. 2016, MNRAS, 459, 3287, `https://doi.org/10.1093/mnras/stw798`

Dalya, G., Frei, Z., Galgoczi, G., Raffai, P., & de Souza, R. S. 2016, VizieR Online Data Catalog, VII/275

Dametto, N. Z., Riffel, R., Colina, L., Riffel, R. A., Piqueras López, J., & et al. 2019, MNRAS, 482, 4437, `https://doi.org/10.1093/mnras/sty2996`

Davis, T. A. 2014, MNRAS, 445, 2378, `https://doi.org/10.1093/mnras/stu1850`

de Vaucouleurs, G., de Vaucouleurs, A., Corwin, Herold G., J., & et al. 1991, Third Reference Catalogue of Bright Galaxies

Di Francesco, J., Johnstone, D., Kirk, H., MacKenzie, T., & Ledwosinska, E. 2008, ApJS, 175, 277, `https://doi.org/10.1086/523645`

Dickman, R. L. 1978, ApJS, 37, 407, `https://doi.org/10.1086/190535`

Erickson, N., Narayanan, G., Goeller, R., & Grosslein, R. A. J. 2007, in ASPC 375, From Z-Machines to ALMA: (Sub)Millimeter Spectroscopy of Galaxies, ed. R. A. J. Baker, J. Glenn, A. I. Harris, J. G. Mangum, & M. S. Yun (ASPC) 71

Esparza-Arredondo, D., Osorio-Clavijo, N., González-Martín, O., & et al. 2020, ApJ, 905, 29, `https://doi.org/10.3847/1538-4357/abc425`

Fazio, G. G., Hora, J. L., Allen, L. E., & et al. 2004, ApJS, 154, 10, `https://doi.org/10.1086/422843`

Filippenko, A. V. & Sargent, W. L. W. 1985, ApJS, 57, 503, `https://doi.org/10.1086/191012`

Frei, Z., Guhathakurta, P., Gunn, J. E., & Tyson, J. A. 1996, AJ, 111, 174, `https://doi.org/10.1086/117771`

Fritz, J., Franceschini, A., & Hatziminaoglou, E. 2006, MNRAS, 366, 767, `https://doi.org/10.1111/j.1365-2966.2006.09866.x`

Gao, Y. & Solomon, P. M. 2004a, ApJS, 152, 63, `https://doi.org/10.1086/383003`

————. 2004b, ApJ, 606, 271, `https://doi.org/10.1086/382999`

García-Burillo, S. IAUS15, From Interstellar Clouds to Star-Forming Galaxies: Universal Processes?, ed. P. Jablonka, P. André, & F. van der Tak, 207, `https://doi.org/10.1017/S1743921316007213`

Graciá-Carpio, J., García-Burillo, S., Planesas, P., & Colina, L. 2006, ApJ, 640, 135, `https://doi.org/10.1086/503361`

Griffin, M. J., Abergel, A., Abreu, A., & et al. 2010, A&A, 518, 3, `https://doi.org/10.1051/0004-6361/201014519`

Hirota, T., Yamamoto, S., Mikami, H., & Ohishi, M. 1998, ApJ, 503, 717, `https://doi.org/10.1086/306032`

Holland, W. S., Robson, E. I., Gear, W. K., & et al. 1999, MNRAS, 303, 659, `https://doi.org/10.1046/j.1365-8711.1999.02111.x`

Hönig, S. F. & Kishimoto, M. 2017, ApJ, 838, 20, `https://doi.org/10.3847/2041-8213/aa6838`

Huchra, J. P., Wyatt, W. F., & Davis, M. 1982, AJ, 87, 1628, `https://doi.org/10.1086/113254`

Iles, E. J., Pettitt, A. R., & Okamoto, T. 2022, MNRAS, 510, 3899, `https://doi.org/10.1093/mnras/stab3330`

Imanishi, M., Baba, S., Nakanishi, K., & Izumi, T. 2023, ApJ, 954, 148, `https://doi.org/10.3847/1538-4357/ace90d`

Israel, F. P. 2020, A&A, 635, 131, `https://doi.org/10.1051/0004-6361/201834198`

Jarrett, T. H., Masci, F., Tsai, C. W., & et al. 2013, AJ, 145, 6, `https://doi.org/10.1088/0004-6256/145/1/6`

Jiang, X., Wang, J., & Gu, Q. 2011, MNRAS, 418, 1753, `https://doi.org/10.1111/j.1365-2966.2011.19596.x`

Jiménez-Bailón, E., Santos-Lleó, M., Mas-Hesse, J. M., et al. 2003, ApJ, 593, 127, `https://doi.org/10.1086/376554`

Jiménez-Donaire, M. J. 2017, PhD thesis, Dense Gads and Interstellar Medium in nearby Galaxies, Ruprecht-Karls University of Heidelberg, Germany

Jiménez-Donaire, M. J., Bigiel, F., Leroy, A. K., et al. 2017, MNRAS, 466, 49, `https://doi.org/10.1093/mnras/stw2996`

————. 2019, ApJ, 880, 127, `https://doi.org/10.3847/1538-4357/ab2b95`

Jones, A. P., Köhler, M., Ysard, N., Bocchio, M., & Verstraete, L. 2017, A&A, 602, 46, `https://doi.org/10.1051/0004-6361/201630225`

Keene, J., Schilke, P., Kooi, J., Lis, D. C., Mehringer, D. M., & Phillips, T. G. 1998, ApJ, 494, 107, `https://doi.org/10.1086/311164`

Kennicutt, R. C. & Evans, N. J. 2012, ARA&A, 50, 531, `https://doi.org/10.1046/annurev-astro-081811-125610`

Kim, S., Rey, S.-C., Jerjen, H., et al. 2014, ApJS, 215, 22, https://doi.org/10.1088/0067-0049/215/2/22

Kohno, K. 2003, ASPC 289, The Proceedings of the IAU 8th Asian-Pacific Regional Meeting, Volume I, ed. S. Ikeuchi, J. Hearnshaw, & T. Hanawa (San Francisco, CA: ASP) 349

Kohno, K., Matsushita, S., Vila-Vilaró, B., Okumura, S. K., & Shibatsuka, T. 2001, ASPC 249, Proceedings, The Central Kiloparsec of Starbursts and AGNS: The La Palma Connection, ed. J. H. Knapen, J. E. Beckman, I. Shlosman, & T. J. Mahoney, (San Francisco CA: ASP), 672

Lang, P., Meidt, S. E., Rosolowsky, E., et al. 2020, ApJ, 897, 122, https://doi.org/10.3847/1538-4357/ab9953

Lee, C., Chung, A., Yun, M. S., et al. 2014, MNRAS, 441, 1363, https://doi.org/10.1093/mnras/stu670

Leroy, A. K., Sandstrom, K. M., Lang, D., et al. 2019, ApJS, 244, 24, https://doi.org/10.3847/1538-4365/ab3925

Leroy, A. K., Schinnerer, E., Hughes, A., et al. 2021, ApJS, 257, 43, https://doi.org/10.3847/1538-4365/ac17f3

Leroy, A. K., Usero, A., Schruba, A., et al. 2017, ApJ, 835, 217, https://doi.org/10.3847/1538-4357/835/2/217

Li, F., Wang, J., Fang, M., et al. 2020, PASJ, 72, 41, https://doi.org/10.1093/pasj/psaa025

Li, F., Wang, J., Gao, F., et al. 2021, MNRAS, 503, 4508, https://doi.org/10.1093/mnras/stab745

Loenen, A. F., Spaans, M., Baan, W. A., & Meijerink, R. 2008, A&A, 488, 5, https://doi.org/10.1051/0004-6361:200810327

Malkan, M. A., Jensen, L. D., Rodriguez, D. R., Spinoglio, L., & Rush, B. 2017, ApJ, 846, 102, https://doi.org/10.3847/1538-4357/aa8302

Martin, D. C., Fanson, J., Schiminovich, D., et al. 2005, ApJ, 619, 1, https://doi.org/10.1086/426387

Martín, S., Kohno, K., Izumi, T., et al. 2015, A&A, 573, 116, https://doi.org/10.1051/004-6361/201425105

Meier, D. S. & Turner, J. L. 2005, ApJ, 618, 259, https://doi.org/10.1086/426499

Meier, D. S., Walter, F., Bolatto, A. D., et al. 2015, ApJ, 801, 63, https://doi.org/10.1088/0004-637X/801/1/63

Meijerink, R. & Spaans, M. 2005, A&A, 436, 397, https://doi.org/10.1051/0004-6361:20042398

Meijerink, R., Spaans, M., & Israel, F. P. 2007, A&A, 461, 793, https://doi.org/10.1051/0004-6361:20066130

Miyaji, T., Herrera-Endoqui, M., Krumpe, M., et al. 2019, ApJ, 884, 10, https://doi.org/10.3847/2041-8213/ab46bc

Morokuma-Matsui, K., Sorai, K., Sato, Y., et al. 2020, PASJ, 72, 90, https://doi.org/10.1093/pasj/psaa084

Moustakas, J. & Kennicutt, Jr., R. C. 2006, ApJS, 164, 81, https://doi.org/10.1086/500971

Nakajima, T., Takano, S., Kohno, K., Harada, N., & Herbst, E. 2018, PASJ, 70, 7, https://doi.org/10.1093/pasj/psx153

Nenkova, M., Sirocky, M., Ivezic, Z., & Elitzur, M. 2008, ApJ, 685, 160, https://doi.org/10.1086/590483

Nenkova, M., Sirocky, M. M., Ivezić, Ž., & Elitzur, M. 2008a, ApJ, 685, 147, https://doi.org/10.1086/590482

Nenkova, M., Sirocky, M. M., Nikutta, R., Ivezić, Ž., & Elitzur, M. 2008b, ApJ, 685, 160, https://doi.org/10.1086/590483

Neugebauer, G., Habing, H. J., van Duinen, R., & et al. 1984, ApJ, 278, 1, https://doi.org/10.1086/184209

Neumann, L., Gallagher, M. J., Bigiel, F., & et al. 2023, MNRAS, 521, 3348, https://doi.org/10.1093/mnras/stad424

Nishimura, Y., Aalto, S., Gorski, M. D., et al. 2024, arXiv:2402.15436, https://doi.org/10.48550/arXiv.2402.15436

Pilbratt, G. L., Riedinger, J. R., Passvogel, T., et al. 2010, A&A, 518, 1, https://doi.org/10.1051/0004-6361/201014759

Poglitsch, A., Waelkens, C., Geis, N., et al. 2010, A&A, 518, 2, https://doi.org/10.1051/0004-6361/201014535

Privon, G. C., Ricci, C., Aalto, S., et al. 2020, ApJ, 893, 149, https://doi.org/10.3847/1538-4357/ab8015

Rahman, N., Helou, G., & Mazzarella, J. M. 2006, ApJ, 652, 1068, https://doi.org/10.1086/508566

Riffel, R. A., Colina, L., Storchi-Bergmann, T., & et al. 2016, MNRAS, 461, 4192, https://doi.org/10.1093/mnras/stw1609

Rybak, M., Hodge, J. A., Greve, T. R., & et al. 2022, A&A, 667, 70, https://doi.org/10.1051/0004-6361/202243894

Salim, S., Boquien, M., & Lee, J. C. 2018, ApJ, 859, 11, https://doi.org/10.3847/1538-4357/aabf3c

Salim, S., Lee, J. C., Janowiecki, S., et al. 2016, ApJS, 227, 2, https://doi.org/10.3847/0067-0049/227/1/2

Sanders, D. B., Mazzarella, J. M., Kim, D.-C., Surace, J. A., & Soifer, B. T. 2003, AJ, 126, 1607, https://doi.org/10.1086/376841

Sandstrom, K. M., Leroy, A. K., Walter, F., et al. 2013, ApJ, 777, 5, https://doi.org/10.1088/0004-637X/777/1/5

Santos, D. J. D., Goto, T., Kim, S. J., et al. 2021, MNRAS, 507, 3070, https://doi.org/10.1093/mnras/stab2352

Schinnerer, E., Maciejewski, W., Scoville, N., & Moustakas, L. A. 2002, ApJ, 575, 826, https://doi.org/10.1086/341348

Sheth, K., Regan, M., Hinz, J. L., et al. 2010, PASP, 122, 1397, https://doi.org/10.1086/657638

Skrutskie, M. F., Cutri, R. M., Stiening, R., & et al. 2006, AJ, 131, 1163, https://doi.org/10.1086/498708

Snell, R. L., Narayanan, G., Yun, M. S., et al. 2011, AJ, 141, 38, https://doi.org/10.1088/0004-6256/141/2/38

Soifer, B. T., Boehmer, L., Neugebauer, G., & Sanders, D. B. 1989, AJ, 98, 766, https://doi.org/10.1086/115178

Solomon, P. M., Downes, D., Radford, S. J. E., & Barrett, J. W. 1997, ApJ, 478, 144, https://doi.org/10.1086/303765

Sorai, K., Kuno, N., & et al. 2019, PASJ, 71, 14, https://doi.org/10.1093/pasj/psz115

Stassun, K. G. 2019, VizieR Online Data Catalog, IV/38

Strong, A. W., Bloemen, J. B. G. M., Dame, T. M., et al. 1988, A&A, 207, 1

Teng, Y.-H., Sandstrom, K. M., Sun, J., et al. 2023, ApJ, 925, 72, https://doi.org/10.3847/1538-4357/ac382f

Teng, Y.-H., Sandstrom, K. M., Sun, J., & et al. 2023, ApJ, 950, 119, https://doi.org/10.3847/1538-4357/accb86

Urry, C. M. & Padovani, P. 1995, PASP, 107, 803, https://doi.org/10.1086/133630

Usero, A., Leroy, A. K., Walter, F., et al. 2015, AJ, 150, 115, https://doi.org/10.1088/0004-6256/150/4/115

Utomo, D., Sun, J., Leroy, A. K., et al. 2018, ApJ, 861, 18, https://doi.org/10.3847/2041-8213/aacf8f

Veron-Cetty, M. P. & Veron, P. 1986, A&AS, 66, 335

Véron-Cetty, M.-P. & Véron, P. 2006, A&A, 455, 773, https://doi.org/10.1051/0004-6361:20065177

Wang, T.-W., Goto, T., Kim, S. J., et al. 2020, MNRAS, 499, 4068, https://doi.org/10.1093/mnras/staa2988

Werner, M. W., Roellig, T. L., Low, F. J., et al. 2004, ApJS, 154, 1, https://doi.org/10.1086/422992

Wilson, T. L. & Rood, R. 1994, ARA&A, 32, 191, https://doi.org/10.1146/annurev.aa.32.090194.001203

Wright, E. L. 2006, PASP, 118, 1711, https://doi.org/10.1086/510102

Wright, E. L., Eisenhardt, P. R. M., Mainzer, A. K., et al. 2010, AJ, 140, 1868, https://doi.org/10.1088/0004-6256/140/6/1868

Wu, J., Evans II, Neal J., Gao, Y., et al. 2005, ApJ, 635, 173, https://doi.org/10.1086/499623

Wu, J., Evans II, Neal J., Shirley, Y. L., & Knez, C. 2010, ApJS, 188, 313, https://doi.org/10.1088/0067-0049/188/2/313

Yajima, Y., Sorai, K., Kuno, N., et al. 2019, PASJ, 71, 13, https://doi.org/10.1093/pasj/psz022

Yamada, S., Ueda, Y., Herrera-Endoqui, M., et al. 2023, ApJS, 265, 37, https://doi.org/10.3847/1538-4365/acb349

Yun, M. S., Aretxaga, I., Gurwell, M. A., et al. 2015, MNRAS, 454, 3485, https://doi.org/10.1093/mnras/stv1963

Yun, M. S., Reddy, N. A., & Condon, J. J. 2001, ApJ, 554, 803, https://doi.org/10.1086/323145

Zurita, A., Florido, E., Bresolin, F., Pérez-Montero, E., & Pérez, I. 2021, MNRAS, 500, 2359, https://doi.org/10.1093/mnras/staa2246

Erika Benítez, I. Cruz-González, Martín Herrera-Endoqui, Yair Krongold, and Ángel A. Soní: Instituto de Astronomía, Universidad Nacional Autónoma de México, Apdo. Postal 70-264, Cd. de México (irene@astro.unam.mx).

Arturo I. Gómez-Ruiz: CONAHCYT-Instituto Nacional de Astrofísica Óptica y Electrónica, Luis E. Erro 1, 72840 Tonantzintla, Puebla, México.

Martín Herrera-Endoqui: Estancia Posdoctoral por México, CONAHCYT, Coordinación de Apoyos a Becarios e Investigadores.